Publication Year	2018
Acceptance in OA@INAF	2020-12-17T19:10:28Z
Title	Radio haloes in nearby galaxies modelled with 1D cosmic ray transport using SPINNAKER
Authors	Heesen, V.; Krause, M.; Beck, R.; Adebahr, B.; Bomans, D. J.; et al.
DOI	10.1093/mnras/sty105
Handle	http://hdl.handle.net/20.500.12386/28969
Journal	MONTHLY NOTICES OF THE ROYAL ASTRONOMICAL SOCIETY
Number	476

Radio haloes in nearby galaxies modelled with 1D cosmic ray transport using SPINNAKER

V. Heesen,[1,2]⋆ M. Krause,[3] R. Beck,[3] B. Adebahr,[3,4,5] D. J. Bomans,[5] E. Carretti,[6,7]
M. Dumke,[3,8] G. Heald,[4,6] J. Irwin,[9] B. S. Koribalski,[6] D. D. Mulcahy,[10]
T. Westmeier[11] and R.-J. Dettmar[5]

[1]*School of Physics and Astronomy, University of Southampton, Southampton SO17 1BJ, UK*

[2]*Universität Hamburg, Hamburger Sternwarte, Gojenbergsweg 112, D-21029 Hamburg, Germany*

[3]*Max-Planck-Institut für Radioastronomie, Auf dem Hügel 69, D-53121 Bonn, Germany*

[4]*ASTRON, the Netherlands Institute for Radio Astronomy, Postbus 2, NL-7990 AA Dwingeloo, the Netherlands*

[5]*Astronomisches Institut der Ruhr-Universität Bochum, Universitätsstr. 150, D-44780 Bochum, Germany*

[6]*CSIRO Astronomy and Space Science, Australia Telescope National Facility, PO Box 76, Epping, NSW 1710, Australia*

[7]*INAF Osservatorio Astronomico di Cagliari, Via della Scienza 5, I-09047 Selargius (CA), Italy*

[8]*European Southern Observatory, Alonso de Cordova 3107, Vitacura, Santiago, Chile*

[9]*Department of Physics, Engineering Physics, & Astronomy, Queen's University, Kingston, ON K7L 3N6, Canada*

[10]*Jodrell Bank Centre for Astrophysics, Alan Turing Building, Oxford Road, Manchester M13 9PL, UK*

[11]*ICRAR, M468, The University of Western Australia, 35 Stirling Highway, Crawley, WA 6009, Australia*

ABSTRACT

We present radio continuum maps of 12 nearby ($D \leq 27$ Mpc), edge-on ($i \geq 76°$), late-type spiral galaxies mostly at 1.4 and 5 GHz, observed with the Australia Telescope Compact Array, Very Large Array, Westerbork Synthesis Radio Telescope, Effelsberg 100-m, and Parkes 64-m telescopes. All galaxies show clear evidence of radio haloes, including the first detection in the Magellanic-type galaxy NGC 55. In 11 galaxies, we find a thin and a thick disc that can be better fitted by exponential rather than Gaussian functions. We fit our SPINNAKER (SPectral INdex Numerical Analysis of K(c)osmic-ray Electron Radio-emission) 1D cosmic ray transport models to the vertical model profiles of the non-thermal intensity and to the non-thermal radio spectral index in the halo. We simultaneously fit for the advection speed (or diffusion coefficient) and magnetic field scale height. In the thick disc, the magnetic field scale heights range from 2 to 8 kpc with an average across the sample of 3.0 ± 1.7 kpc; they show no correlation with either star formation rate (SFR), SFR surface density (Σ_{SFR}), or rotation speed (V_{rot}). The advection speeds range from 100 to 700 km s^{-1} and display correlations of $V \propto \mathrm{SFR}^{0.36\pm0.06}$ and $V \propto \Sigma_{\mathrm{SFR}}^{0.39\pm0.09}$; they agree remarkably well with the escape velocities ($0.5 \leq V/V_{\mathrm{esc}} \leq 2$), which can be explained by cosmic ray-driven winds. Radio haloes show the presence of disc winds in galaxies with $\Sigma_{\mathrm{SFR}} > 10^{-3}\,\mathrm{M}_\odot\,\mathrm{yr}^{-1}\,\mathrm{kpc}^{-2}$ that extend over several kpc and are driven by processes related to the distributed star formation in the disc.

Key words: radiation mechanisms: non-thermal – methods: numerical – cosmic rays – galaxies: haloes – galaxies: magnetic fields – radio continuum: galaxies.

1 INTRODUCTION

This paper is a follow-up study of our recent paper about the 'Advective and diffusive cosmic ray transport in galactic haloes' (Heesen et al. 2016, hereafter HD16), where we presented 1D cosmic ray transport models now implemented in the software SPINNAKER (SPectral INdex Numerical Analysis of K(c)osmic-ray Electron Radio-emission).[1] We have extended our previous radio continuum observations of two edge-on galaxies, adding another 10 galaxies, to study advection speed, magnetic field scale height, and diffusion coefficient across a wider range of galactic parameters. We then study the influence of the star formation rate (SFR), SFR surface density (Σ_{SFR}), and rotation speed (V_{rot}) on these results. We use

---

⋆E-mail: volker.heesen@hs.uni-hamburg.de

[1] www.github.com/vheesen/Spinnaker

Table 1. General properties of our sample galaxies.

Galaxy	i^a (°)	d_{25}^b (arcmin)	D^c (Mpc)	M_B^d (mag)	Type^e	Nucleus^f	SFR^g ($M_\odot$ yr^{-1})	$r_\star^h$ (kpc)	$\log_{10}(\Sigma_{SFR})^i$ ($M_\odot$ yr^{-1} kpc^{-2})	$\log_{10}(M_{tot})^j$ ($M_\odot$)	V_{rot}^k (km s^{-1})
NGC 55	80.0	34.1	1.9	−18.89	SBm		0.16	6.2	−2.87	10.26	91
NGC 253	78.5	25.8	3.9	−20.64	SABc	H II	6.98	11.8	−1.80	11.16	205
NGC 891	89.0	12.2	10.2	−20.09	Sb	H II	4.72	11.7	−1.96	11.28	212
NGC 3044	90.0	4.4	18.7	−19.53	SBc		2.03	9.8	−2.17	10.81	153
NGC 3079	88.0	7.7	19.7	−20.94	SBcd	Sy2	9.09	13.3	−1.79	11.35	208
NGC 3628	87.0	14.8	7.9	−20.01	Sb	T2	1.73	10.7	−2.32	11.26	215
NGC 4565	90.0	16.2	24.7	−22.37	Sbc	Sy1.9	5.69	37.1	−2.88	11.91	244
NGC 4631	85.0	14.7	6.9	−20.12	SBcd	H II	2.89	12.1	−2.20	10.82	138
NGC 4666	76.0	4.2	26.6	−21.14	SABc	LINER	16.19	14.0	−1.58	11.15	193
NGC 5775	84.0	3.9	26.9	−20.71	Sbc	H II	9.98	14.4	−1.81	11.09	187
NGC 7090	89.0	6.8	10.6	−19.70	Sc		0.62	7.2	−2.41	10.57	124
NGC 7462	90.0	5.0	13.6	−18.57	SBbc		0.28	7.5	−2.80	10.46	112

Notes. Data are from Tully & Fisher (1988) unless otherwise noted. Available on Vizier (http://vizier.cfa.harvard.edu).
^{a}Inclination angles were measured from kinematic analysis of the H I line in NGC 55 (Westmeier, Koribalski & Braun 2013) and in NGC 891 (Oosterloo, Fraternali & Sancisi 2007), and in NGC 253 of the Balmer H α line (Pence 1981). They have uncertainties of $\pm 1°$. In the remaining galaxies, they have been measured by Tully & Fisher (1988, NGC 3044–5775) and Karachentsev, Makarov & Kaisina (2013, NGC 7090 and 7462) from the ratio of the minor to major axis assuming an intrinsic disc height. They have larger uncertainties, typically $\pm 3°$.
^{b}Optical diameter measured at the 25 mag arcsec^{-2} isophote in the *B* band.
^{c}Distances are from the NASA/IPAC Extragalactic Database (NED; Virgo infall only), assuming $H_0 = 73$ km s^{-1}. For the most nearby galaxies NGC 55 and 253, we used the distances from Pietrzyński et al. (2006, NGC 55) and Karachentsev et al. (2003, NGC 253), who used the Cepheid period–luminosity relation and the tip of the red giant branch, respectively.
^{d}Absolute *B*-band magnitude from Tully & Fisher (1988) and corrected to our distances.
^{e}Galaxy morphological classification.
^{f}Optical classification of the nuclear spectrum, from Ho, Filippenko & Sargent (1997) where Sy = Seyfert and T = transition object. The classification of NGC 253 is based on the assumption that the nuclear activity is starburst dominated (Westmoquette, Smith & Gallagher 2011). The classification of NGC 4666 is from Veilleux et al. (1995).
^{g}Star formation rate is SFR $= 0.39 \times L_{TIR}/10^{43}$ erg s^{-1}, where L_{TIR} is the 3–1100 μm total infrared luminosity. The conversion factor is from Kennicutt & Evans (2012) and has an uncertainty of 0.3 dex. See Appendix A for details which infrared data were used.
^{h}Radius of the actively star-forming disc (within the last ≈ 100 Myr), estimated from the radial extent of the radio continuum emission. A cross-check of six galaxies with *GALEX* far-UV (FUV) catalogue by Gil de Paz et al. (2007) found agreement within 10 per cent.
^{i}SFR surface density is $\Sigma_{SFR} = \text{SFR}/(\pi r_\star^2)$. The uncertainty is 0.3 dex.
^{j}Total masses are calculated $M_{tot} = 0.233 \cdot R_{kpc} \cdot V_{rot,100}^2 \times 10^{10} \, M_\odot$, where R_{kpc} is the radius of the galaxy estimated from d_{25} using the distance *D* and $V_{rot,100}$ is the rotation speed in units of 100 km s^{-1}. They have uncertainties of 0.1 dex.
^{k}Maximum rotation speeds are from Westmeier et al. (2013, NGC 55), Pence (1981, NGC 253), Oosterloo et al. (2007, NGC 891), the HyperLeda data base (http://leda.univ-lyon1.fr, NGC 3044–5775; Makarov et al. 2014), and Dahlem et al. (2005, NGC 7090 and 7462). They have uncertainties of ± 3 km s^{-1}.

a combination of so far unpublished and archival data from the Australia Telescope Compact Array (ATCA), the Very Large Array (VLA), and the Westerbork Synthesis Radio Telescope (WSRT). For a sub-sample of four galaxies, we use single-dish observations with both the Effelsberg 100-m and Parkes 64-m telescopes in order to complement the interferometric data. The majority of the interferometric observations were taken before the recent upgrade of the correlators, so that we mostly use 100-MHz bandwidths, rather than the GHz bandwidths that are available nowadays. While this leads to reduced sensitivities of tens rather than a few μJy beam^{-1}, a sample like this is a good reference against which to compare the new wide-band data as observed with the Karl G. Jansky VLA (Wiegert et al. 2015).

Our sample contains 12 nearby edge-on galaxies (11 late-type spiral galaxies and one Magellanic-type galaxy), which lie in the SFR range of $0.1 \leq \text{SFR}/(M_\odot \text{ yr}^{-1}) \leq 16$. Where possible, we produce maps that have a spatial resolution of 1 kpc or better. The reason for this is to allow the separation of the thin and thick radio disc, which are present in most galaxies. The thin disc (with a scale height of a few 100 pc) represents a region of current/recent star formation populated by supernova (SN) remnants and H II regions (Ferrière 2001); the thick disc (with a scale height of a few kpc) is what we refer to in this work as the 'halo' and represents the region of extra-planar gas, magnetic fields, and cosmic rays with

no ongoing star formation (Rossa & Dettmar 2003a; Krause et al. 2017). As we will show in this paper, we observe a transition between thin and thick disc at a height of $|z| \approx 1$ kpc, so that we will refer to the halo as emission at $|z| \gtrsim 1$ kpc. We are aware that the transition between the disc and halo is gradual (the 'disc–halo' interface), and the observed transition will also depend on the spatial resolution.[2]

Most of our sample galaxies have been studied in the radio (continuum and line) in detail before, so we will give here only a brief summary of their most notable properties (general properties are summarized in Table 1). NGC 55, a Magellanic-type (irregular, of intermediate mass between dwarf and spiral galaxies) galaxy and member of the Sculptor group, has a very thick H I disc extending up to a height of 10 kpc into the halo (Westmeier et al. 2013). Thick H I discs could be a sign of a galactic fountain or ongoing gas accretion. NGC 253, another member of the Sculptor group, is a prototypical nuclear starburst galaxy and is most notable

---

[2] In this paper, we are using 'thick disc' and 'halo' in a synonymous way. Strictly speaking, the thick disc extends all the way to the mid-plane because it is a second component that we see superposed on to the thin disc. In contrast, the halo refers to heights above ≈ 1 kpc, excluding everything closer to the mid-plane.

for its 'dumbbell-shaped' radio halo caused by strong synchrotron cooling in the centre of the galaxy (Heesen et al. 2009a,b, 2011). This galaxy is also notable for a very bright X-ray halo, which shows the presence of a 'disc wind', which is unrelated to the nuclear outflow (Bauer et al. 2008). The distinction between nuclear outflows and disc winds is important for this study: nuclear outflows emanate from the central few 100 pc driven by a combination of concentrated star formation and jets from active galactic nuclei (AGNs). In our work, we concentrate on the disc winds, which extend over a large fraction of the star-forming disc over several kpc at least, although the scale can be smaller than 10 kpc (see Westmoquette et al. 2011, for a discussion of nuclear outflows versus disc winds).

NGC 891 has a prominent thick H I disc, the kinematics of which have been studied in detail by Oosterloo et al. (2007). They showed that this galaxy still accretes intergalactic matter, so that the halo is only in part caused by the galactic fountain. NGC 891 is the best case to study the influence of ongoing accretion on to a radio halo. NGC 3044 hosts a large H I supershell that extends to a height of 3 kpc above the mid-plane (Lee & Irwin 1997). These H I supershells require dozens of SNe and are essential for an active disc–halo interface. We expect these kinds of features to be abundant in our galaxies, but the spatial resolution of our observations is not high enough to resolve these features.

NGC 3079 is a case in point for a galaxy with a nuclear outflow driven by a combination of starburst and low-luminosity AGN. Jets from the AGN entrain the surrounding material, which is subsequently transported away from the nucleus (Middelberg et al. 2007; Shafi et al. 2015). Above and below the nucleus, there are well-defined kpc-sized lobes of non-thermal emission, surrounded by filamentary H α emission that have counterparts in X-ray emission (Cecil et al. 2001; Cecil, Bland-Hawthorn & Veilleux 2002). While the filamentary emission is clearly connected to the nuclear outflow and AGN-driven jets, there are also indications for a disc wind in this galaxy. First, there are vertical H α and dust filaments extending over the full extent of the disc (Cecil et al. 2001), reminiscent of a 'boiling disc' in NGC 253 (Sofue, Wakamatsu & Malin 1994), which is indicative of an active disc–halo interface. Secondly, the X-ray emission in the halo extends, as in NGC 253, for several kpc away from the nuclear outflow (Strickland et al. 2004); it is questionable that the two are related. In order to study the disc wind only, we have masked the radio continuum emission stemming from the nuclear outflow in the following analysis.

NGC 3628, a nuclear starburst galaxy, is a member of the Leo Triplet and possesses a 140-kpc long tidal tail of atomic hydrogen detected in the 21-cm H I line (Haynes, Giovanelli & Roberts 1979). NGC 4565 has a 'lagging' H I halo, where the rotational velocity of the neutral gas decreases with increasing distance from the mid-plane. This makes it likely that this galaxy has an ongoing galactic fountain, in spite of the galaxy having only little extra-planar H I emission (Zschaechner et al. 2012). NGC 4631 is the galaxy with arguably the most prominent radio halo. This is in part caused by gravitational interaction with its neighbour NGC 4656, where a 'spur' of ordered magnetic fields leads to the neighbour galaxy (Hummel et al. 1988; Mora & Krause 2013). This merger has probably caused a starburst in the past that led to an outflow, the result of which we see now (Irwin et al. 2011). NGC 4666 is a starburst galaxy with outflowing ionized H α emission (Dahlem et al. 1997; Voigtländer et al. 2013), while NGC 5775 is the prototypical X-shaped halo magnetic field galaxy (Tüllmann et al. 2000; Soida et al. 2011). These galaxies have magnetic field structures that look in projection like an 'X'. The field shapes are thought to be caused by either a galactic dynamo in the halo or

by the interaction of the magnetic field lines with a galactic wind (Heesen et al. 2009b). Finally, NGC 7090 and NGC 7462 are rather unremarkable galaxies, although both possess a layer of extra-planar H α and H I emission (Rossa & Dettmar 2003a,b; Dahlem et al. 2005).

In this paper, we present observations at *L*, *C*, and *X* band (1.4, 5, and 8.5 GHz) in order to study vertical profiles of the non-thermal intensities and the non-thermal radio spectral index. We use exponential and Gaussian functions to model the vertical profiles of the non-thermal radio emission. These profiles are then fitted with our cosmic ray transport models, in order to measure advection speeds, diffusion coefficients, and magnetic field scale heights. We estimate magnetic field strengths from energy equipartition (Beck & Krause 2005) and use the total infrared luminosity to determine photon energy densities. Thus, we can take both the synchrotron and inverse Compton (IC) losses of the cosmic ray electrons (CREs) into account.

This paper is organized as follows: in Section 2, we describe our observations and data reduction techniques. In Section 3, we motivate and present our cosmic ray transport models. Results are presented in Section 4, followed by the discussion in Section 5. We finish off with our conclusions in Section 6. Fig. 2 shows the radio continuum maps for NGC 4631, followed by Figs 3 and 4, which contain a step-by-step guide on how we obtained the best-fitting cosmic ray transport model for this particular galaxy. Fig. 5 summarizes the results for our sample with an atlas of maps and models presented in Appendix D. Throughout the paper, the radio spectral index α is defined in the sense $S_\nu \propto \nu^\alpha$ and quantities averaged across the sample are error weighted and presented with an uncertainty of $\pm 1\sigma$.

2 OBSERVATIONS AND DATA REDUCTION

2.1 Radio continuum maps

We used a variety of radio continuum observations, most of them already published, which we obtained from the respective telescope archives. We re-reduced these data, which we describe in the following. In Table 2, we present a summary of the observations used, including references where the data were published first.

2.1.1 Australia Telescope Compact Array

Observations of NGC 55 with the ATCA were calibrated following standard procedures with MIRIAD (Sault, Teuben & Wright 1995), where we set the flux density of the primary calibrator J1938−634 with MFCAL (part of MIRIAD). At *L* band, we combined previously published data from Wells (1997) with newly obtained data as part of the Local Volume H I Survey. At *C* band, we used again the previously published data of Wells (1997) and added new observations; these data were observed in 2008 November and 2009 February in the radio continuum mode with a bandwidth of 256 MHz, split into two intermediate frequencies (IFs) of 128 MHz bandwidth each. More data were observed in 2010 with the upgraded Compact Array Broad-band Backend (Wilson et al. 2011) receiver (4.7–6.6 GHz). Because NGC 55 has an angular extension that exceeds the primary beam both at *L* and *C* band, we used several pointings to mosaic the galaxy. The calibrated (*u*, *v*) data were precessed to J2000.0 if necessary and exported into the FITS format. The observations and data reduction of NGC 7090 and 7462 were already presented in HD16.

Table 2. Observation details for the galaxies presented in this paper.

Galaxy	Band[a]	ν[b] (GHz)	Telescope[c]	Configuration[d]	Project[e]	Time[f] (h)	Date[g]	Notes[h]	Reference[i]
NGC 55	L	1.37	ATCA	750D	C287	8.7	1993 Aug 1	Mosaic	17
...	...	...	...	375	C287	11.2	1995 Jan 12	...	...
...	...	...	...	750A	C287	11.1	1995 Oct 25	...	...
...	...	...	...	H75	C1341	5.0	2005 Jul 17	Mosaic	This work
...	...	...	...	EW352	C1341	9.4	2005 Oct 7	...	...
...	C	4.80	...	375	C287	3.6	1994 Mar 29	Mosaic	17
...	...	...	...	375	C287	10.2	1994 Mar 30	...	...
...	...	...	...	375	C287	7.8	1994 Mar 31	...	...
...	...	...	...	375	C287	12.5	1994 Nov 23	...	...
...	...	...	...	750A	C287	5.1	1995 Mar 1	...	...
...	...	...	...	375	C287	5.3	1995 Aug 16	...	...
...	...	...	...	375	C287	10.2	1995 Nov 24	...	...
...	...	4.67	...	EW352	C1974	7.6	2008 Nov 22	...	This work
...	...	...	...	EW364	C1974	9.9	2009 Feb 13	...	...
...	C	5.60	...	H168	C1974	7.6	2010 Mar 27	...	...
...	C	4.80	Parkes	single-dish	P697	16.0	2010 Oct 7	Merged	...
NGC 253	L	1.46	VLA	B+C+D	AC278	4.1	1990 Sep–1991 Mar	Mosaic	2
...	C	4.86	...	D	AH844	35.8	2004 Jul 4–24	Mosaic	10
...	...	4.85	Effelsberg	single-dish	N/A	N/A	1997	Merged	...
NGC 891	L	1.39	WSRT	Multiple	R02B	240	2002 Aug–Dec		13
...	C	4.86	VLA	D	AA94	11.2	1988 Aug 29		16
...	...	4.85	Effelsberg	single-dish	44–95	9.1	1996 Feb–Aug		6
NGC 3044	L	1.49	VLA	B	AI28	3.1	1986 Aug 1		This work
...	...	...	...	C	AI23	0.8	1985 Jul 25		11
...	...	...	...	D	AI31	1.1	1987 Apr 28/30		...
...	C	4.86	...	C	AB676	0.8	1993 Jun 13		4
...	...	...	...	D	AM573	1.1	1997 Nov 6		This work
...	...	...	...	D	AI31	1.0	1987 Apr 28		11
NGC 3079	L	1.66	VLA	B	BS44	1.0	1997 Mar 8		This work
...	...	1.41	...	CD	BS44	2.4	1997 Oct 2		...
...	...	1.43	...	C	AB740	1.3	1996 Feb 17		...
...	C	4.71	...	C	AC277	3.9	1990 Dec 9		3
...	...	4.86	...	D	AD177	2.5	1986 Jan 16		This work
NGC 3628	L	1.49	VLA	CD	AS300	4.3	1988 Mar 25		14
...	...	...	...	D	AS300	8.4	1987 Apr 7		...
...	C	4.86	...	D	AK243	7.7	1991 Mar 28		7
NGC 4565	L	1.49	VLA	B	AS326	3.8	1988 Jan 29		16
...	...	1.48	...	D	AS326	10.6	1988 Aug 28		...
...	C	4.86	...	D	AK424	3.4	1996 Sep 28		6
NGC 4631	L	1.37	WSRT	maxi-short	N/A	6.0	2003 Apr 3		1
...	C	4.86	VLA	D	AH369	12.1	1989 Nov 22/26	Mosaic	9
...	...	...	...	D	AD896	4.3	1999 Apr 14	Mosaic	12
...	...	4.85	Effelsberg	single-dish	55–94	6.3	1996 Feb–Aug	Merged	6
NGC 4666	L	1.43	VLA	CD	AD346	3.5	1994 Nov 20		5
...	...	1.49	...	D	AS199	0.2	1984 Aug 31		This work
...	C	4.86	...	D	AD326	12.5	1993 Dec 20/24		5
NGC 5775	L	1.49	VLA	B	AI0028	3.2	1986 Aug 1		8
...	...	1.48	...	B	AB492	1.2	1989 Aug 4		...
...	...	1.49	...	C	AH368	3.6	1990 Nov 19/24		...
...	...	...	...	D	AI31	1.9	1987 Apr 27/30		11
...	X	8.45	...	D	AD455	13.4	2001 Dec 14		15

[a]Observing band.

[b]Observing centre frequency.

[c]Telescope.

[d]Configuration of the interferometer or single-dish telescope (the maxi-short configuration of the WSRT allows for optimum imaging performance for very extended sources within a single track observation).

[e]Project ID.

[f]On-source time.

[g]Observation date.

[h]Comments [some interferometric observations were done in mosaic mode and the single-dish maps were merged with the interferometric maps (Section 2.1.5)].

[i]Reference where the data were first published. For all entries, '...' stands for an identical entry as above and 'N/A' denotes an entry that is not available. Details for the observations of NGC 7090 and 7462 can be found in HD16.

References. (1) Braun et al. (2007); (2) Carilli et al. (1992); (3) Cecil et al. (2001); (4) Colbert et al. (1996); (5) Dahlem et al. (1997); (6) Dumke (1997); (7) Dumke & Krause (1998); (8) Duric, Irwin & Bloemen (1998); (9) Golla & Hummel (1994); (10) Heesen et al. (2009a); (11) Irwin, English & Sorathia (1999); (12) Mora & Krause (2013); (13) Oosterloo et al. (2007); (14) Reuter et al. (1991); (15) Soida et al. (2011); (16) Sukumar & Allen (1991); (17) Wells (1997).

2.1.2 *Very Large Array*

Observations with the VLA were calibrated following standard procedures with AIPS.[3] We set the flux density of the primary calibrator (either 3C 48 or 286) according to the model by Baars et al. ([1977]). Since the data were observed only with the 'historical' VLA prior to the upgrade of the correlator, observations had bandwidths of 100 MHz split into two IFs of 50 MHz each. We used data at *L* band (NGC 253, 3044, 3079, 3628, 4565, 4666, and 5775), *C* band (NGC 253, 891, 3044, 3079, 3628, 4565, 4631, and 4666), and *X* band (NGC 5775). We used maps of NGC 253 published earlier without either re-calibrating or re-imaging of the data. The observations at *L* and *C* band were already described in Carilli et al. ([1992]) and Heesen et al. ([2009a]), respectively. The calibrated data were precessed to J2000.0 where necessary and exported into the FITS format.

2.1.3 *Westerbork Synthesis Radio Telescope*

We used a 1.4-GHz map of NGC 891 observed with the WSRT, which was already presented by Oosterloo et al. ([2007]). Furthermore, we used the 1.4-GHz map of NGC 4631 again observed with the WSRT. This galaxy was observed as part of the WSRT SINGS survey (Braun et al. [2007]), and we re-imaged the map as described below.

2.1.4 *Single-dish telescopes*

In order to correct for the missing 'zero-spacing flux', we use additional *C*-band maps from the Effelsberg 100-m telescope (NGC 253, 891, 4631) and from the Parkes 64-m telescope (NGC 55).[4] The Effelsberg maps have been published before (see Table [2] for references), but the Parkes map is so far unpublished, so we describe these observations here in more detail. Observations with the *C* band AT Multi-band receiver (4.5–5.1 GHz) were carried out in 2010 September. Maps were taken in standard fashion using the 'basket weaving' procedure with scans alternating in the right ascension and declination directions. The data were calibrated with scans in azimuth and elevation of the primary calibrator J1938−634, before they were combined using the single-dish mapping algorithm described in Carretti et al. ([2010]). The resulting Parkes map of NGC 55 is presented in Appendix C along with the Effelsberg maps of NGC 253, 891, and 4631.

2.1.5 *Imaging*

We imported the calibrated (u, v) data into the Common Astronomy Software Applications (CASA; McMullin et al. [2007]) and formed and deconvolved images of them using the multi-scale multi-frequency algorithm in the *clean* task (Rau & Cornwell [2011]). We did not use the frequency dependence of the sky model (nterms=1) because this is not necessary for our small fractional bandwidths (mostly

<10 per cent). The obvious exception is the ATCA data, where the fractional bandwidth is highest with 34 per cent. But because we created a 'joint deconvolution' mosaic (Sault, Staveley-Smith & Brouw [1996]) in CASA (imagermode=mosaic), we could not use the frequency dependence; this option can thus far not be combined with a frequency-dependent sky model (nterms $\geq$ 2). Since we do not detect any obvious artefacts left over after the deconvolution, we think that our approach is sufficient for our data.[5] We used the multi-scale option with angular scales ranging typically between one synthesized beam size and the size of the galaxy. We cleaned the maps down to 2σ, where σ is the rms noise level. Finally, we applied the primary beam correction.

We deconvolved one map with CLEAN using Briggs weighting (robust=0) and adjusted the weighting of the other map to robust values between 0 and 0.5, in order to have a similar resolution. For NGC 55 and 4631, we had several pointings of a mosaic. They were processed within CASA using the joint deconvolution option of the CLEAN algorithm. Maps were imported back into AIPS to convolve them to a common circular beam and re-grid them to the same coordinate system, for which we used PARSELTONGUE (Kettenis et al. [2006]) to batch process them. The *C*-band maps of NGC 55 and 4631 were combined with the single-dish maps from the Parkes and Effelsberg telescopes, respectively, using the *imerg* task in AIPS. The *C*-band map of NGC 891 had no flux missing since the single-dish and interferometric integrated fluxes were in good agreement, so that we did not merge it with the Effelsberg map. The properties of the radio maps are summarized in Tables [3] and [4].

2.1.6 *Integrated flux densities*

We integrated the flux densities of our galaxies using rectangular boxes with *imstat* in AIPS. Highly inclined galaxies have box-shaped radio haloes (rather than elliptical haloes), so that this method is the most suitable one (rather than integrating in ellipses as for moderately inclined galaxies). The angular extent of the radio emission along the major and minor axis, which is the region that encompasses the 3σ contour line of the most sensitive map, can be found in Table [4]. We chose the box size to integrate the emission to be slightly larger than this region, checking that the choice has only little influence ($\leq$2 per cent).

We checked the integrated flux densities (Table [3]) of our maps and found most of them to agree within 5 per cent with published values in the literature (Table [5]). These values are interferometric measurements at *L* band and single-dish measurements at *C* band (so that missing fluxes play no role). We detect significantly higher (50 per cent) flux densities in NGC 55 at both *L* and *C* bands. At *L* band, our observations have a better (u, v) coverage than the comparison snapshot observation with the VLA by Condon et al. ([1996]), so that we are less affected by the missing zero-spacing flux. At *C* band, the flux density of Wright et al. ([1994]) is integrated in an area with a major axis of only 7 arcmin, whereas the source size detected by us is 24 arcmin; faint, diffuse emission was missed so that the flux density is lower. Other notable exceptions are NGC 4565, where we detect a 20 per cent higher flux density at *L* band, and NGC 4666, where our *C*-band flux density is 15 per cent lower than the literature value. In the case of NGC 4565, it is likely that we

---

[3] AIPS, the Astronomical Image Processing System, is free software available from the National Radio Astronomy Observatory.

[4] Radio interferometers are only sensitive to emission not exceeding a certain angular scale, which is related to the shortest baseline for which visibilities are measured. The (u, v) plane has no measurements at a baseline of zero length, which can be only measured with a single-dish telescope. This is needed to measure the true integrated flux density. The difference between the interferometric and single-dish flux density is hence usually referred to as the 'missing zero-spacing' flux.

[5] We do not advocate this procedure as generally the best deconvolution technique for mosaicked observations. Depending on the data, a linear mosaic (e.g. using *ltess* in AIPS) of the individual pointings deconvolved with nterms=2 may give a better result.

Table 3. Radio properties of our sample galaxies.

Galaxy	$\Theta_{\mathrm{FWHM}}^{a}$ (arcsec)	ν_1^{b}	ν_2^{b} (GHz)	S_1^{c} (Jy)	$S_{1,\mathrm{nt}}^{d}$ (Jy)	S_2^{c} (Jy)	$S_{2,\mathrm{nt}}^{d}$ (Jy)	α^{e}	α_{nt}^{f}
NGC 55	41.10	1.36	5.56	0.6082 ± 0.0172	0.5219 ± 0.0152	0.2966 ± 0.0107	0.2216 ± 0.0084	-0.51 ± 0.03	-0.61 ± 0.03
NGC 253	30.00	1.46	4.85	6.3000 ± 0.1409	6.2133 ± 0.1390	2.7100 ± 0.0678	2.6331 ± 0.0659	-0.70 ± 0.03	-0.72 ± 0.03
NGC 891	17.30	1.39	4.86	0.7720 ± 0.0155	0.7663 ± 0.0154	0.2720 ± 0.0056	0.2670 ± 0.0056	-0.83 ± 0.02	-0.84 ± 0.02
NGC 3044	7.80	1.49	4.86	0.1040 ± 0.0021	0.0990 ± 0.0020	0.0450 ± 0.0009	0.0406 ± 0.0009	-0.71 ± 0.02	-0.75 ± 0.03
NGC 3079	8.30	1.53	4.71	0.8360 ± 0.0169	0.8262 ± 0.0167	0.3430 ± 0.0350	0.3342 ± 0.0341	-0.79 ± 0.09	-0.80 ± 0.09
NGC 3628	17.70	1.49	4.86	0.5482 ± 0.0198	0.5433 ± 0.0196	0.2287 ± 0.0051	0.2243 ± 0.0050	-0.74 ± 0.04	-0.75 ± 0.04
NGC 4565	13.10	1.49	4.86	0.1599 ± 0.0116	0.1585 ± 0.0115	0.0557 ± 0.0012	0.0544 ± 0.0013	-0.89 ± 0.06	-0.90 ± 0.06
NGC 4631	23.10	1.37	4.86	1.2850 ± 0.0287	1.2451 ± 0.0283	0.4654 ± 0.0251	0.4303 ± 0.0236	-0.80 ± 0.05	-0.84 ± 0.05
NGC 4666	15.70	1.45	4.86	0.3870 ± 0.0087	0.3712 ± 0.0083	0.1370 ± 0.0039	0.1230 ± 0.0035	-0.86 ± 0.03	-0.91 ± 0.03
NGC 5775	8.25	1.49	8.46	0.2680 ± 0.0097	0.2630 ± 0.0095	0.0598 ± 0.0022	0.0556 ± 0.0020	-0.86 ± 0.03	-0.89 ± 0.03
NGC 7090	13.80	1.38	4.67	0.0563 ± 0.0030	0.0519 ± 0.0029	0.0153 ± 0.0023	0.0114 ± 0.0018	-1.07 ± 0.13	-1.24 ± 0.14
NGC 7462	13.90	1.38	4.67	0.0256 ± 0.0009	0.0238 ± 0.0012	0.0066 ± 0.0002	0.0050 ± 0.0006	-1.10 ± 0.04	-1.27 ± 0.11

Notes. Uncertainties quoted in this table were calculated as explained in Section 2.4.

[a]Angular resolution, referred to as the full width at half-maximum (FWHM), of the circular synthesized beam.

[b]Observing frequencies ν_1 and ν_2.

[c]Integrated flux densities, S_1 and S_2, at observing frequencies ν_1 and ν_2.

[d]Non-thermal integrated flux densities, $S_{1,\mathrm{nt}}$ and $S_{2,\mathrm{nt}}$, after the subtraction of the thermal radio continuum emission (Section 2.2).

[e]Integrated radio spectral index between ν_1 and ν_2.

[f]Integrated non-thermal radio spectral index between ν_1 and ν_2.

Table 4. Further radio properties of our sample galaxies.

Galaxy	d_{maj}^{a}	d_{min}^{a} (arcmin)	PA^{b} (°)	σ_1^{c}	σ_2^{c} (μJy beam^{-1})	W_{stripe}^{d} (arcmin)	W_{stripe}^{d} (kpc)	Stripe centre^{e}
NGC 55	24.0	9.3	108.0	130	40	24.6	14.0	RA $00^{\mathrm{h}}15^{\mathrm{m}}07\overset{\mathrm{s}}{.}637$ Dec. $-39°12'58\overset{''}{.}46$
NGC 253	21.9	11.3	52.0	250	30	20.3	24.0	RA $00^{\mathrm{h}}47^{\mathrm{m}}33\overset{\mathrm{s}}{.}190$ Dec. $-25°17'16\overset{''}{.}14$
NGC 891	10.9	5.9	23.0	23	22	4.9	15.0	RA $02^{\mathrm{h}}22^{\mathrm{m}}33\overset{\mathrm{s}}{.}118$ Dec. $+42°20'54\overset{''}{.}88$
NGC 3044	3.9	2.2	114.0	30	24	2.7	15.0	RA $09^{\mathrm{h}}53^{\mathrm{m}}40\overset{\mathrm{s}}{.}953$ Dec. $+01°34'45\overset{''}{.}50$
NGC 3079	4.5	2.1	167.0	81	23	4.4	26.0	RA $10^{\mathrm{h}}01^{\mathrm{m}}57\overset{\mathrm{s}}{.}695$ Dec. $+55°40'48\overset{''}{.}80$
NGC 3628	11.0	5.3	105.0	80	22	4.6	11.0	RA $11^{\mathrm{h}}20^{\mathrm{m}}16\overset{\mathrm{s}}{.}642$ Dec. $+13°35'21\overset{''}{.}76$
NGC 4565	13.7	2.8	135.5	26	25	7.6	56.0	RA $12^{\mathrm{h}}36^{\mathrm{m}}20\overset{\mathrm{s}}{.}911$ Dec. $+25°59'11\overset{''}{.}95$
NGC 4631	13.3	8.1	86.0	35	50	5.8	12.0	RA $12^{\mathrm{h}}42^{\mathrm{m}}07\overset{\mathrm{s}}{.}164$ Dec. $+32°32'32\overset{''}{.}18$
NGC 4666	4.3	2.5	40.0	50	20	3.6	29.0	RA $12^{\mathrm{h}}45^{\mathrm{m}}08\overset{\mathrm{s}}{.}707$ Dec. $-00°27'44\overset{''}{.}23$
NGC 5775	4.1	2.4	145.0	35	15	3.6	29.0	RA $14^{\mathrm{h}}53^{\mathrm{m}}57\overset{\mathrm{s}}{.}526$ Dec. $+03°32'42\overset{''}{.}35$
NGC 7090	5.4	3.5	128.0	28	13	2.7	8.5	RA $21^{\mathrm{h}}36^{\mathrm{m}}28\overset{\mathrm{s}}{.}774$ Dec. $+54°33'26\overset{''}{.}70$
NGC 7462	3.8	1.9	73.0	25	9	2.9	12.0	RA $23^{\mathrm{h}}02^{\mathrm{m}}46\overset{\mathrm{s}}{.}751$ Dec. $+40°50'08\overset{''}{.}09$

Notes. [a]Extent of the radio continuum emission along the major and minor axes.

[b]Position angle of the major axis.

[c]rms map noises at observing frequencies ν_1 and ν_2.

[d]Stripe width to measure the vertical intensity profile in arcmin and kpc.

[e]Central position of the stripe in J2000.0 coordinates.

have detected more flux since we have used a 12-h-long observation in D-configuration, whereas the literature value of Condon et al. (2002) is based on an NRAO VLA Sky Survey (NVSS) snapshot observation. NGC 4666 has an optical size of 4.6 arcmin, which is comparable to the largest angular scale (LAS) detectable at *C* band with the VLA (5 arcmin) in D-configuration, so that it is possible that we have missed some flux.

Notably, our other *C*-band flux densities agree within 5 per cent with single-dish data, so that missing zero spacings are not an issue for us. At *L* band, we see indications of missing flux in NGC 55 and NGC 253. In these two galaxies, the spectral index is affected by missing flux in *L* band, which in NGC 55 causes a flat spectral index in the northern halo and in NGC 253 a flat spectral index for distances exceeding 4 kpc from the mid-plane. We restrict our spectral index analysis to the unaffected areas. In the remaining

galaxies at *L* band, we do not expect it to be an issue. The largest galaxy of those is NGC 4565, which has an optical angular size of 16.2 arcmin. This galaxy has been measured with a 12 h long integration with the VLA in D-array, where the LAS is 16 arcmin, so that missing flux is likely not an issue here.

2.2 Thermal radio continuum maps

To correct for the contribution of thermal radio continuum emission, we used Balmer Hα line observations following the procedure described in Heesen et al. (2014). Where no Hα map was available, we used a *Spitzer* 24-μm map instead and scaled it to a published Hα flux density (NGC 3628, 4565, and 4666). The *Spitzer* mid-infrared map traces the dust-obscured star formation, so that we cannot expect a good Hα–mid-infrared correlation on a spatially

Table 5. Literature flux densities.

Galaxy	ν_1	ν_2	S_1	S_2	Reference
	(GHz)		(mJy)		(ν_1/ν_2)
NGC 55	1.49	4.85	381	197	3/10
NGC 253	1.46	4.85	6300	2710	7/7
NGC 891	1.40	4.85	701	286	4/8
NGC 3044	1.40	4.85	114	43	9/5
NGC 3079	1.40	4.85	865	321	4/1
NGC 3628	1.40	4.85	525	247	4/8
NGC 4565	1.40	4.80	134	54	4/8
NGC 4631	1.37	4.80	1290	476	2/8
NGC 4666	1.40	4.85	434	161	4/6
NGC 5775	1.40	4.85	284	94	4/8

References. (1) Becker, White & Edwards (1991); (2) Braun et al. (2007); (3) Condon et al. (1996); (4) Condon, Cotton & Broderick (2002); (5) Gregory & Condon (1991); (6) Griffith et al. (1995); (7) Heesen et al. (2009a); (8) Stil et al. (2009); (9) White & Becker (1992); (10) Wright et al. (1994).

resolved basis. But since we are averaging (radially and along the line of sight) over several kpc in order to measure the vertical profiles of the non-thermal radio continuum, the exact distribution does not matter for our study. Also, we find that the thermal radio continuum contribution at *C* band is typically less than 10 per cent in the halo, where our study is focused (at *L* band it is even lower). The non-thermal radio spectral index is hence only by a value of 0.06 systemically steeper between 1.4 and 4.85 GHz (steepening from $\alpha = -1.00$ to -1.06, for instance) than the total radio spectral index. This is similar to the size of our error bars on the radio spectral index, so that the contribution of the thermal radio continuum emission is actually not that important in the halo. Consequently, we do not expect the difference between the Balmer Hα and *Spitzer* mid-infrared map to make a large difference for our analysis.

This can also be seen when considering that the thermal contribution to the radio continuum intensity at 1.4 GHz (it varies slowly with frequency as $\nu^{-0.1}$) is

$$I_{\mathrm{th},1.4} = 2.5 \times 10^{-9} \cdot \mathrm{EM} \cdot \Theta_{\mathrm{FWHM}}^2 \ \mathrm{Jy\,beam^{-1}}, \tag{1}$$

where EM is the Hα emission measure in units of cm pc^{-6} and Θ_{FWHM} is the angular resolution of the radio map, referred to as the full width at half-maximum, in units of arcsec. The above relation is obtained when combining equation 2 from Voigtländer et al. (2013) with equation 4 from Heesen et al. (2014), assuming an electron temperature of $T_e = 10^4$ K and an integration area of $\Omega = 1.133 \cdot \Theta_{\mathrm{FWHM}}^2$ arcsec^2. Typically, the emission measure drops below 100 cm pc^{-6} at a height of 1 kpc, so that at 10 arcsec resolution the thermal radio continuum intensity is smaller than 25 µJy beam^{-1} (Collins et al. 2000), similar to the rms noise of our maps. The emission measure drops even further at larger heights (the scale heights are only $\approx$0.5 kpc) and the thermal contribution becomes entirely negligible.

We corrected our maps for foreground absorption using $E(B - V)$ values, but these corrections are only a few per cent (it is largest for NGC 891 with 15 per cent). We do not correct for internal absorption by dust (internal to the observed galaxy) except in NGC 3079 and 4666, where the Balmer decrement has been used to estimate it (Voigtländer et al. 2013). The correction is a factor of 2.4 in NGC 3079 and 2.9 in NGC 4666; hence, it totally dominates the estimate of the Hα flux. But since the absorption by dust is negligible in the halo (Collins et al. 2000), we do not have to correct for internal absorption. Hence, we have possibly overcorrected the thermal flux

in NGC 3079 and 4666, but the fractions are low ($<$10 per cent). We also do not correct for the contribution of [N II], which in our sample is between 25 (NGC 55) and 45 per cent (NGC 4666). Using the absolute *B*-band magnitude as proxy (Kennicutt et al. 2008), we expect an average of 35 per cent of [N II] contribution; this means we slightly overestimate the thermal radio continuum emission.[6] We conclude that the thermal contribution is negligible in the halo and our measurements of the non-thermal intensities are conservative *lower* limits.

2.3 Masking

We masked unrelated background sources, which we identified as point-like sources in the halo that have no counterpart in the Hα map. Furthermore, we masked nuclear starbursts and AGNs in those galaxies that have a prominent, dominating nucleus in the radio continuum maps (NGC 253, 3079, and 3628). In NGC 3079, we have masked the nuclear outflow as well, as far as we could distinguish it from the remainder of the disc and halo emission. In NGC 891, we have masked emission from SN1986J (Rupen et al. 1987). For all galaxies, the same mask was then applied to all maps (radio continuum at both frequencies and thermal radio continuum) before the construction of the spectral index maps.

2.4 Uncertainties

The errors of the integrated flux densities were calculated with two contributions. First, we assumed a 2 per cent relative calibration error for the WSRT and VLA observations (Braun et al. 2007; Perley & Butler 2013). For the single-dish observations, the calibration error is also 2 per cent for the Parkes observations at *C* band (Griffith & Wright 1993) and for the Effelsberg observations at *C* and *X* band (Beck, private communication). Secondly, we added the uncertainty arising from the baselevel error, which is $\sigma_N = \sigma_b N = \sigma\sqrt{N}$, where N is the number of beams within the integration region and the baselevel uncertainty for the intensities is $\sigma_b = \sigma/\sqrt{N}$. This is a crude estimate since if an image contains large-scale artefacts due to insufficient calibration (interferometric data) or due to scanning effects (single-dish data), the rms variation in the image, σ, is larger than just thermal noise and does not have Gaussian characteristics. Hence, we checked this error by measuring the average flux intensity in areas surrounding the galaxies, where the box size was selected to be similar to the galaxy size and found approximate agreement. The calibration and background errors were quadratically added with $(\delta S_\nu)^2 = (\epsilon_S S_\nu)^2 + \sigma_N^2$, where $\epsilon_S = 0.02$. For the subtraction of the thermal emission, we used the error of the Hα flux density, which was then propagated into the non-thermal flux densities and spectral indices.

For our main analysis, we created vertical profiles of the radio continuum intensity averaged in stripes. The stripes were spaced by $0.5 \cdot \theta_{\mathrm{FWHM}} \cdot D$ in the vertical direction and had stripe widths between 0.5 and 1.0 of the length of the major axis (see Table 4 for the stripe widths). For the vertical intensity profiles, we used a 5 per cent calibration error, owing to the calibration uncertainty and the deconvolution process. The error contributions are again added in quadrature $(\delta I_\nu)^2 = (\epsilon_I I_\nu)^2 + \sigma_b^2$, with $\epsilon_I = 0.05$. This uncertainty neglects the variation of the intensities within stripe

---

[6] The [N II] emission line falls into the bandpass of the Hα filter; the contribution from this emission cannot be separated from the Hα flux, which is hence an overestimate.

width; the reason is that we assume in the following a 1D approach of cosmic ray transport and any variation as a function of galactocentric radius is not included in our model. The error of the radio spectral index is then calculated with the following equation:

$$\Delta\alpha = \frac{1}{\ln\left(\frac{\nu_1}{\nu_2}\right)} \cdot \sqrt{\left(\frac{\delta I_1}{I_1}\right)^2 + \left(\frac{\delta I_2}{I_2}\right)^2}, \qquad (2)$$

where δI_1 and δI_2 are the intensity errors and I_1 and I_2 the intensities at the observing frequencies ν_1 and ν_2, respectively.

3 COSMIC-RAY TRANSPORT MODELS

3.1 Motivation

3.1.1 Key assumptions

Our goal is to study the vertical cosmic ray transport using the 1D models for pure advection and diffusion from HD16. These models assume that the CREs are injected at a galactic height of $z = 0$ and then transported away from the disc by either pure advection in a galactic wind or by diffusion along vertical magnetic field lines. We use these models with the following two assumptions.

(i) We fit the radio spectral index in the halo only. This is motivated by the fact that the vertical profiles of the radio spectral index are not affected by the limited angular resolution for heights $|z| \gtrsim 1$ kpc, and the correction for thermal radio continuum emission becomes negligible.

(ii) We model the magnetic field as a two-component exponential function with a thin and a thick disc. This is motivated by the fact that in most galaxies the vertical non-thermal intensity profiles can be best fitted by a two-component exponential function (e.g. Dahlem, Dettmar & Hummel 1994; Oosterloo, Fraternali & Sancisi 2007; Heesen et al. 2009a; Soida et al. 2011; Mora & Krause 2013). Exceptions can be explained by low angular resolution and inclination angles, or by a diffusion-dominated cosmic ray transport, which causes Gaussian intensity profiles (HD16).
We discuss these assumptions in more detail in Sections 3.1.2 and 3.1.3. The 1D treatment is motivated by the many studies of cosmic ray-driven winds that have used the 'flux tube' approximation (e.g. Breitschwerdt, McKenzie & Völk 1991, 1993; Everett et al. 2008; Dorfi & Breitschwerdt 2012; Recchia, Blasi & Morlino 2016b). They assume straight, open magnetic field lines rising above the disc. In this geometry, the wind flows along a tube of approximately constant cylindrical cross-section up to a height $z \approx z_{\mathrm{break}}$, after which the area increases (usually assumed to scale as $\propto z^2$) and hence the magnetic field strength decreases as well. Everett et al. (2008) found $z_{\mathrm{break}} = 4.5$ kpc in the Milky Way, which is of the order of the scale height of the magnetic field (Haverkorn & Heesen 2012). These models have been able to reproduce the X-ray data in the Milky Way and nearby galaxies, where it was shown that the wind speed in the halo is of the order of the escape velocity and its value does not change by more than a factor of a few (Everett et al. 2008; Breitschwerdt et al. 2012). This is important, because we assume a constant advection speed that is able to describe the data to first order. We note that choosing a constant advection speed will give the minimum magnetic field strength in the halo. An accelerating flow dilutes the CRE number density by longitudinal expansion and adiabatic losses (Heesen et al. 2018), so that the magnetic field estimate would have to increase in order to fit the observed intensities.
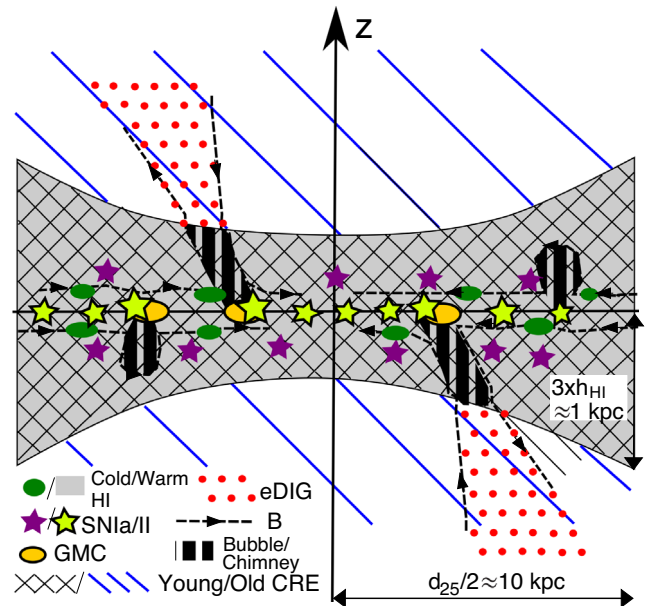

Figure 1. A diagram of the disc–halo interface in galaxies with $\Sigma_{\mathrm{SFR}} \ll 10^{-1}$ M$_\odot$ yr^{-1} kpc^{-2}. CREs are injected in the disc plane by Type II SNe (and Type Ib/Ic) and in the halo by Type Ia SNe. They accumulate in superbubbles that can break out from the flaring disc of warm H I and form a 'chimney', which are cospatial with plumes of extra-planar diffuse ionized gas (eDIG). The magnetic field (dashed lines with arrows) is anchored to the disc in the cold H I clouds. The vertical scale is stretched by a factor of 5.

3.1.2 Disc–halo interface

This paper is about haloes, but in order to investigate them, we need to take into account the full vertical extent of a galaxy, so we give here a brief overview of the vertical structure of the interstellar medium (ISM). In the context of radio haloes, the transition from the thin to the thick disc is important, so we start with what is commonly referred to as the disc–halo interface. In Fig. 1, we show a conceptual diagram of the disc–halo interface and we discuss in the following how our model can fit into this picture. This diagram is most realistic (although still very simplifying) for galaxies with low $\Sigma_{\mathrm{SFR}} \ll 10^{-1}$ M$_\odot$ yr^{-1} kpc^{-2}, where cosmic rays are most likely to play a role in launching a wind. Galaxies with higher Σ_{SFR} have thermally driven so-called superwinds (Heckman et al. 2000), which are not included in our study (see Adebahr et al. 2013, for a radio continuum study of the superwind galaxy M82).

Cosmic rays are accelerated and injected into the ISM via SNe, where the ejected shells have speeds of the order of $10\,000$ km s^{-1}, which create a strong shock while sweeping up material and slowing down. The turbulent magnetic field lines, which surround the shock, deflect the cosmic rays, resulting in an efficient Fermi type I acceleration with the cosmic rays crossing the shock many times (Bell 1978). On average, the kinetic energy per SN is 10^{51} erg, a few per cent of which is used for the acceleration of cosmic rays (e.g. Rieger, de Oña-Wilhelmi & Aharonian 2013). Of the energy stored in the cosmic rays, between 1 and 2 per cent goes into the CREs with the rest into protons and heavier nuclei (e.g. Beck & Krause 2005). The SNe can be either Type Ia (thermonuclear detonation) or Type II (core-collapse, also Types Ib and Ic). This is of significance since the SNe of Type Ia can occur at galactic heights of a few 100 pc, whereas SNe of other types are restricted to within 100 pc

from the mid-plane (effectively, the scale height of the molecular gas; Ferrière 2001).

In the thin disc, the CRE population is very diverse. Approximately 10 per cent of the radio continuum emission stems from individual SN remnants, with the remaining 90 per cent made up by the diffuse emission (Lisenfeld & Völk 2000). The radio spectral index varies strongly between the spiral arms and the inter-arm regions, which is caused by spectral ageing of the CREs with increasing distance from star formation sites (Tabatabaei et al. 2013a; Heesen et al. 2014). Furthermore, CREs can be found within superbubbles, which can be observed during later stages as H I holes with sizes ranging from 100 pc to 2 kpc (Bagetakos et al. 2011). They are the result of dozens of SNe and some of them can contain the CREs long enough that they display a curved non-thermal radio continuum spectrum (Heesen et al. 2015). They may also be the site of 'chimneys', where star formation activity in the disc drives advective hot gas flows upwards into the halo, carrying magnetic fields along with the hot gas motion and forming cavities in the disc that are observable as H I holes (Heald 2012). We would expect at any given time a few dozens of superbubbles per galaxy with a diameter of a few 100 pc, so that the volume porosity is a few per cent but can be up to 20 per cent (Bagetakos et al. 2011). It hence becomes clear that the CREs in the thin disc are in fact a superposition of many spectral ages (young CREs in the vicinity of star-forming regions, old CREs in the inter-arm regions, young and old CREs in non-thermal superbubbles). Consequently, the radio spectral index of the thin disc is not equivalent to the injection energy spectral index of the CREs as expected from theory, which is $\gamma_{\rm inj} \approx 2$, where the CRE number density is a power law as a function of energy $N \propto E^{-\gamma_{\rm inj}}$, but is steeper. Indeed, the integrated non-thermal radio continuum spectrum of galaxies between 1 and 10 GHz has a spectral index of $\alpha_{\rm nt} \approx -1$, which corresponds to $\gamma_{\rm inj} = 3$ (Niklas, Klein & Wielebinski 1997; Heesen et al. 2014; Basu et al. 2015; Tabatabaei et al. 2017).

In the thick disc, the CRE population becomes more uniform since the distance to the star-forming sites becomes more similar and the contrast between spiral arm and inter-arm regions diminishes. The height at which the transition from thin to thick disc happens is probably of the order of a few 100 pc; this is related to the scale height $h_{\rm HI}$ of the warm H I disc and thus to the largest height the superbubbles can expand to before they blow out (at $z = 3 \times h_{\rm HI}$; Mac Low & Ferrara 1999). The H I discs show a flaring, where the scale height increases with galactocentric distance ($h_{\rm HI} = 100$–500 pc; Bagetakos et al. 2011), so that the superbubble blow-out would occur at heights between 0.3 and 1.5 kpc.

As we will show below, we see the transition from thin to thick disc at a height of 1–2 kpc as traced by a change of the slope in the radio spectral index. Since we cannot really resolve the thin disc, we can only probe the upper limit of the transition height, but our measured values are at least consistent with the described picture. Our first assumption is hence that we fit the radio spectral index in the halo only. In the mid-plane, the radio continuum emission can be described by a power law with an 'injection' spectral index, where this is effectively the spectral index of the diffuse non-thermal radio continuum emission.

3.1.3 Magnetic field structure

The magnetic field in galaxy discs is in approximate energy equipartition with the turbulent gas motions of the (almost) neutral gas and its associated kinetic energy density (Beck 2016). If the magnetic

field is associated with the warm H I disc, as suggested by the superbubble picture, the resulting scale height would be 0.2–1.0 kpc in the thin disc as the magnetic field scale height is a factor of 2 higher than the magnetic pressure scale height.[7] The magnetic field scale height in the thick disc is larger; from equipartition estimates, the scale heights are of the order of 4–8 kpc. It is unclear whether the field is associated with either the hot X-ray emitting gas, which has similar scale heights (Strickland et al. 2004; Hodges-Kluck & Bregman 2013), or the thick H I disc that is seen in some galaxies with scale heights of 2–4 kpc (Zschaechner, Rand & Walterbos 2015; Vollmer, Nehlig & Ibata 2016). We caution though that in both cases accretion from the intergalactic medium probably plays a role as well, so that part of the gas in the halo has a different origin from the magnetic field that is generated by processes *within* the galaxy.

A discussion of the magnetic field structure would be incomplete without mentioning the results from polarization. The halo field consists of a turbulent and ordered component, with the ordered component having the larger scale height. The turbulent component possibly stems from Parker-type loops, which form when buoyant superbubbles inflated with cosmic rays rise from the disc and opposing magnetic field lines reconnect at its base. This allows a closed magnetic field line to detach from the disc magnetic field (Parker 1992). In that case, the trajectory of the loop would be ballistic, such as for clouds of H I gas in a 'Galactic fountain'. The ordered magnetic field could be from blown-out superbubbles, where the magnetic field opens up in the halo, with overlapping bubbles in the thick disc creating the halo field (Heald 2012; Mao et al. 2015; Mulcahy, Beck & Heald 2017). An alternative scenario is that the turbulent magnetic field is generated in the thin disc by the small-scale dynamo, driven by star formation-related turbulence, and advected into the halo by the wind. A lateral pressure gradient or a galactic wind would then be able to shape the field lines into the often observed X-shaped pattern (e.g. Dahlem et al. 1997; Tüllmann et al. 2000; Krause, Wielebinski & Dumke 2006; Heesen et al. 2009b; Krause 2009; Soida et al. 2011; Mora & Krause 2013; Chyży et al. 2016). Such a magnetic field structure has been also seen in models of lagging magnetized haloes (Henriksen & Irwin 2016). Of course, our simple model cannot take all of this into account, and we attempt in this work only to fit for the total magnetic field strength in the halo, neglecting this sub-division.

Our second assumption is hence that the magnetic field strength can be described by a two-component exponential function. In the thin disc, the magnetic field strength is regulated by the pressure of the warm H I gas, which has an exponential distribution. This is expected for a constant velocity dispersion in a constant gravity field as found near the mid-plane. In the thick disc, the dominating turbulent magnetic field is in pressure equilibrium with either the hot X-ray emitting gas or the thick H I disc. If the halo gas is in a hydrostatic equilibrium, the density distribution is close to an exponential function. This is corroborated by observations of the soft X-ray emission in nearby galaxies, which showed that the vertical distribution of the hot ionized gas can be best described by an exponential function, rather than a Gaussian or a power-law function (Strickland et al. 2004). This suggests that X-ray haloes are 'hot atmospheres' surrounding galaxies. If the magnetic field is frozen into the ionized plasma, the magnetic field strength will

---

[7] For an exponential magnetic field distribution $B \propto \exp{(-z/h_{\rm B1})}$, the magnetic energy density is $U_{\rm B} = B^2/(8\pi) \propto \exp{(-2z/h_{\rm B1})}$.

Table 6. Physical properties of our sample galaxies.

Galaxy	L_{TIR}^a $(10^{43}$ erg s$^{-1})$	B_0^b (μG)	U_{TIR}^c	U_{IRF}^d $(10^{-13}$ erg cm$^{-3})$	U_{B}^e	$U_{\text{IRF}}/U_{\text{B}}^f$	$U_{\text{rad}}/U_{\text{B}}^g$	$F_{\text{H}\alpha}^h$ $(10^{12}$ erg s^{-1} cm$^{-2})$	$E(B-V)^i$ (mag)	Ref. Hα Map/Flux
NGC 55	0.41	7.9	0.6	1.6	24.5	0.07	0.24	78.1 ± 3.6	0.012	2/5
NGC 253	17.90	14.0	7.1	19.5	78.3	0.25	0.30	79.0 ± 3.6	0.017	5/5
NGC 891	12.10	14.7	4.9	13.4	86.0	0.16	0.20	5.1 ± 1.1	0.058	7/5
NGC 3044	5.20	13.1	3.0	8.2	68.1	0.12	0.18	4.5 ± 0.5	0.025	7/7
NGC 3079	23.30	19.9	7.3	20.0	157.5	0.13	0.15	9.0 ± 0.4	0.361	11/6
NGC 3628	4.43	12.6	2.2	5.9	63.1	0.09	0.16	4.5 ± 0.4	0.020	24 μm/7
NGC 4565	14.60	8.7	0.6	1.6	29.8	0.05	0.19	1.3 ± 0.4	0.015	24 μm/8
NGC 4631	7.40	13.5	2.8	7.7	72.3	0.11	0.16	36.1 ± 5.0	0.017	5/5
NGC 4666	41.50	18.2	11.9	32.4	132.3	0.24	0.28	14.4 ± 0.6	0.028	24 μm/10
NGC 5775	25.60	16.3	6.9	18.8	105.9	0.18	0.22	4.5 ± 0.5	0.037	1/4
NGC 7090	1.60	9.8	1.7	4.8	38.2	0.12	0.23	4.0 ± 0.6	0.020	5/5
NGC 7462	0.72	9.7	0.7	2.0	37.1	0.05	0.16	1.6 ± 0.8	0.009	9/3

Notes. See Appendix A for details how we calculated the presented values.

^{a}Total infrared luminosity 3–1100 μm from *Spitzer* and *IRAS* data.

^{b}Magnetic field strength in the disc plane, calculated from energy equipartition using BFIELD (Beck & Krause 2005), available at http://www3.mpifr-bonn.mpg.de/staff/mkrause/.

^{c}Total infrared photon energy density, calculated from the total infrared luminosity.

^{d}Radiation energy density of the IRF, excluding the contribution from the CMB.

^{e}Magnetic energy density $U_{\text{B}} = B_0^2/(8\pi)$.

^{f}Ratio of the energy densities of the IRF (excluding the contribution from the CMB) to that of the magnetic field.

^{g}Ratio of the energy densities of the total IRF (including the CMB) to that of the magnetic field.

^{h}Balmer Hα line flux, corrected for foreground absorption.

^{i}The $E(B-V)$ values are from NED to calculate the foreground absorption as $A_V = 2.59 \times E(B-V)$ mag.

References. (1) Collins et al. (2000); (2) (Bomans et al., private communication); (3) HD16; (4) James et al. (2004); (5) Kennicutt et al. (2008); (6) Moustakas & Kennicutt (2006); (7) Rand et al. (2011); (8) Robitaille et al. (2007), (9) Rossa & Dettmar (2003a); (10) Voigtländer et al. (2013); (11) Young et al. (1996). Where no Hα map was available, we used a *Spitzer* 24-μm map instead (marked as 24 μm) from Dale et al. (2009, NGC 3628) and Bendo, Galliano & Madden (2012, NGC 4565 and 4666).

relate to the ionized gas density, so that exponential magnetic fields can be expected.

3.2 Cosmic-ray transport equations

We are using 1D transport equations for the CRE number density $N(E, z)$, where E is the CRE energy and z is the distance to the mid-plane. We assume a fixed inner boundary condition with $N(E, 0) = N_0 E^{-\gamma_{\text{inj}}}$, where γ_{inj} is the injection CRE energy spectral index and N_0 is a normalization constant. The transport equation for advection is

$$\frac{\partial N(E, z)}{\partial z} = \frac{1}{V} \left\{ \frac{\partial}{\partial E} [b(E) N(E, z)] \right\} \quad \text{(Advection)}, \quad (3)$$

where V is the advection speed, assumed here to be constant. Similarly, for diffusion, we have

$$\frac{\partial^2 N(E, z)}{\partial z^2} = \frac{1}{D} \left\{ \frac{\partial}{\partial E} [b(E) N(E, z)] \right\} \quad \text{(Diffusion)}, \quad (4)$$

where we parametrize the diffusion coefficient as a function of the CRE energy as $D = D_0 E_{\text{GeV}}^\mu$, with E_{GeV} being the CRE energy in units of GeV and D_0 the diffusion coefficient at 1 GeV. We assume $\mu = 0.5$ in agreement with what is used for modelling the Milky Way (Strong, Moskalenko & Ptuskin 2007). There is some debate as to whether this energy dependence applies to CREs with energies of a few GeV (e.g. Mulcahy et al. 2016; Recchia, Blasi & Morlino 2016a), but using $\mu = 0$ instead changes the results only slightly and we cannot distinguish with our data one way or the other (see

also HD16). The combined synchrotron and IC loss rate for CREs is given by (e.g. Longair 2011)

$$-\left(\frac{\text{d}E}{\text{d}t}\right) = b(E) = \frac{4}{3} \sigma_{\text{T}} c \left(\frac{E}{m_{\text{e}} c^2}\right)^2 (U_{\text{rad}} + U_{\text{B}}), \quad (5)$$

where U_{rad} is the radiation energy density, U_{B} is the magnetic field energy density, $\sigma_{\text{T}} = 6.65 \times 10^{-25}$ cm^2 is the Thomson cross-section, and $m_{\text{e}} = 511$ keV c^{-2} is the electron rest mass.

The radiation energy density is the sum of the cosmic microwave background (CMB) radiation energy density and the interstellar radiation field (IRF) energy density; the latter includes contributions from starlight radiation energy density and the total infrared radiation energy density from emission by dust. The magnetic field strength B_0 in the mid-plane was calculated from energy equipartition (Beck & Krause 2005). The energy density of the magnetic field is then $U_{\text{B}} = B^2/(8\pi)$. Furthermore, we assumed that the ratio $U_{\text{IRF}}/U_{\text{B}}$ is constant everywhere. The resulting values of these calculations can be found in Table 6, and the details of the calculations are explained in Appendix A.

We assume a two-component exponential magnetic field distribution:

$$B(z) = B_1 \cdot \exp(-|z|/h_{\text{B1}}) + (B_0 - B_1) \cdot \exp(-|z|/h_{\text{B2}}). \quad (6)$$

Here, h_{B1} and h_{B2} are the magnetic field scale heights in the thin and thick disc, respectively, B_0 is the magnetic field strength in the mid-plane, and B_1 is the magnetic field strength of the thin disc component. Equations (3) and (4) are integrated numerically from the inner boundary, so that no outer boundary condition is required. In order to calculate the non-thermal radio continuum intensities,

the CRE number density is convolved with the synchrotron emission profile of an individual CRE (see HD16 for details).

3.3 Fitting procedure

3.3.1 Vertical intensity profiles

In this section, we outline the fitting procedure of the cosmic ray transport models, where we present a step-by-step analysis of NGC 4631. In Fig. 2, we show the radio continuum maps of NGC 4631 – a galaxy that has one of the most impressive radio haloes. We have created vertical profiles of the non-thermal radio continuum intensity, which we present in Fig. 3(a).

In our work, the scale height of the thin disc is comparable to the spatial resolution of the maps. This is why, we use the analytical functions of Dumke et al. (1995) that convolve the Gaussian point spread function (PSF) with either exponential or Gaussian intensity distributions. This Gaussian PSF is exact for interferometric maps and it is a good approximation for single-dish maps. Furthermore, it has become 'standard practice' to include a contribution of the inclined disc (if $i < 90°$), measuring a Gaussian radio intensity distribution along the major axis and projecting that on to the minor axis. This larger PSF is then referred to as the 'effective beam' (e.g. Heesen et al. 2009a; Adebahr et al. 2013).

We fit two-component exponential and Gaussian functions to vertical non-thermal intensity profiles, which we present as solid and dashed lines, respectively (see Appendix B for details). For this galaxy, a two-component exponential function fits better than a two-component Gaussian function with a reduced $\chi^2_{exp} = 0.4$ as opposed to $\chi^2_{Gauss} = 3.0$ (average of the northern and southern halo at both frequencies). Using the fits to the data, we create vertical non-thermal intensity model profiles using either of the two frequencies, depending on which data have the better quality. We calculate the error bars using the uncertainties of the maxima and scale heights of the thin and thick discs (see Appendix B for details).

In Fig. 3(b), we show the vertical profile of the non-thermal spectral index in NGC 4631. The spectral index is fairly flat in the mid-plane with $\alpha \approx -0.7$ and steepens in the halo to values of $\alpha \approx -1.4$. The profile shows a conspicuous 'shoulder', where the spectral index slope flattens at heights $|z| \gtrsim 1$ kpc. This distance corresponds to the transition from the thin to the thick disc seen in the intensity profiles. We note that the slope of the spectral index profile cannot be resolved in the thin disc because the effective beam is too large. Furthermore, we are overestimating the non-thermal radio spectral index in the thin disc since we did not correct the Balmer H α line emission for internal absorption due to dust (Section 2.2). In the halo, however, these influences can be neglected, so that we can study the spectral index profile there. In order to illustrate the influence of the effective beam, we have shown its contribution to the vertical intensity profile in Fig. 3(a); in the case of NGC 4631, we restrict the fitting of the spectral index to $|z| \geq 1.4$ kpc. We show the fitting areas for the rest of the sample in Appendix D. In NGC 55 and 253, the fitting area also has an outer limit, because the *L*-band maps are affected by missing fluxes (Section 2.1.6). In NGC 253, we do not exclude this thin disc in the fit since we do not resolve it in the spectral index anyway and there would be otherwise not enough data points for a meaningful fit.

3.3.2 Finding the best-fitting model

We simultaneously fit for the advection speed (or diffusion coefficient), the magnetic field scale height, and the injection spectral index. In order to find an 'initial guess', we first vary the magnetic field profile to fit the intensity model at one frequency, varying the scale height and choosing an advection speed (or diffusion coefficient) that approximately fits the spectral index profile (together with the chosen injection spectral index). For NGC 4631, we show the best-fitting advection intensity profile in Fig. 3(c) and the best-fitting advection spectral index profile in Fig. 3(b). The corresponding vertical profile of the magnetic field strength is shown in Fig. 3(d). The error interval of the latter stems from the uncertainties of the magnetic field scale heights in the thin and thick disc; it does not include any uncertainty from the total magnetic field strength estimate from the equipartition assumption (we discuss the influence of the equipartition estimate in Section 5.3). The magnetic field strength decreases rapidly and reaches a value of approximately half the maximum field strength at $|z| = 1$ kpc from where on it decreases more slowly.

From the best-fitting model, we can work out the uncertainties of the advection speed and magnetic field strength. This is shown in Fig. 4, where we plot the reduced χ^2 for both the intensity and spectral index fitting in NGC 4631. The fitting of the intensities depends almost exclusively on the magnetic field profile, although a higher advection speed can offset a lower magnetic field scale height. In contrast, the fitting of the spectral index profile depends mostly on the advection speed and hardly on the magnetic field scale height. This means that best-fitting areas are almost perpendicularly aligned, so that the advection speed and magnetic field scale height can be constrained well by a simultaneous fit.

4 RESULTS

In Table 7, we present non-thermal intensity scale heights in the thick disc at *L* and *C* band, magnetic field scale heights in the thin and thick discs, advection speeds, and diffusion coefficients for the entire sample. In some cases, we could find a best-fitting value for the magnetic field scale height and/or advection speed, but not an upper and/or lower limit. For these values, the given error interval is a lower limit; they are plotted in Fig. 5 for the parameter studies with arrows denoting the error bars, but are not taken into account for the statistical analysis. Maps and plots are presented in Appendix D.

4.1 The distinction between advection and diffusion

At first, we present our findings whether the cosmic ray transport in haloes is advection or diffusion dominated. We note that this distinction is a common one since advection will take over diffusion in the halo quickly if there is a galactic wind (Ptuskin et al. 1997; Recchia et al. 2016b). The effective boundary $s_\star$ at which ($|z| > s_\star$) advection dominates over diffusion is

$$\frac{s_\star^2}{D} \approx \frac{s_\star}{V} \Rightarrow s_\star \approx 0.3 \times \frac{D_{28}}{V_{100}} \text{ kpc}, \tag{7}$$

where D_{28} is the diffusion coefficient in units of 10^{28} cm^2 s^{-1} and V_{100} is the advection speed in units of 100 km s^{-1}. Diffusion coefficients in galaxies have values of a few 10^{28} cm^2 s^{-1} (e.g. Berkhuijsen, Beck & Tabatabaei 2013; Tabatabaei et al. 2013b; Mulcahy et al. 2014, 2016) in agreement with the Milky Way value of 3×10^{28} cm^2 s^{-1} (Strong et al. 2007). For a diffusion coefficient of 3×10^{28} cm^2 s^{-1} and an advection speed of 200 km s^{-1}, the transition happens at a height of 0.45 kpc. Hence, it is justified to assume an advection-only model in the halo if there is a wind.
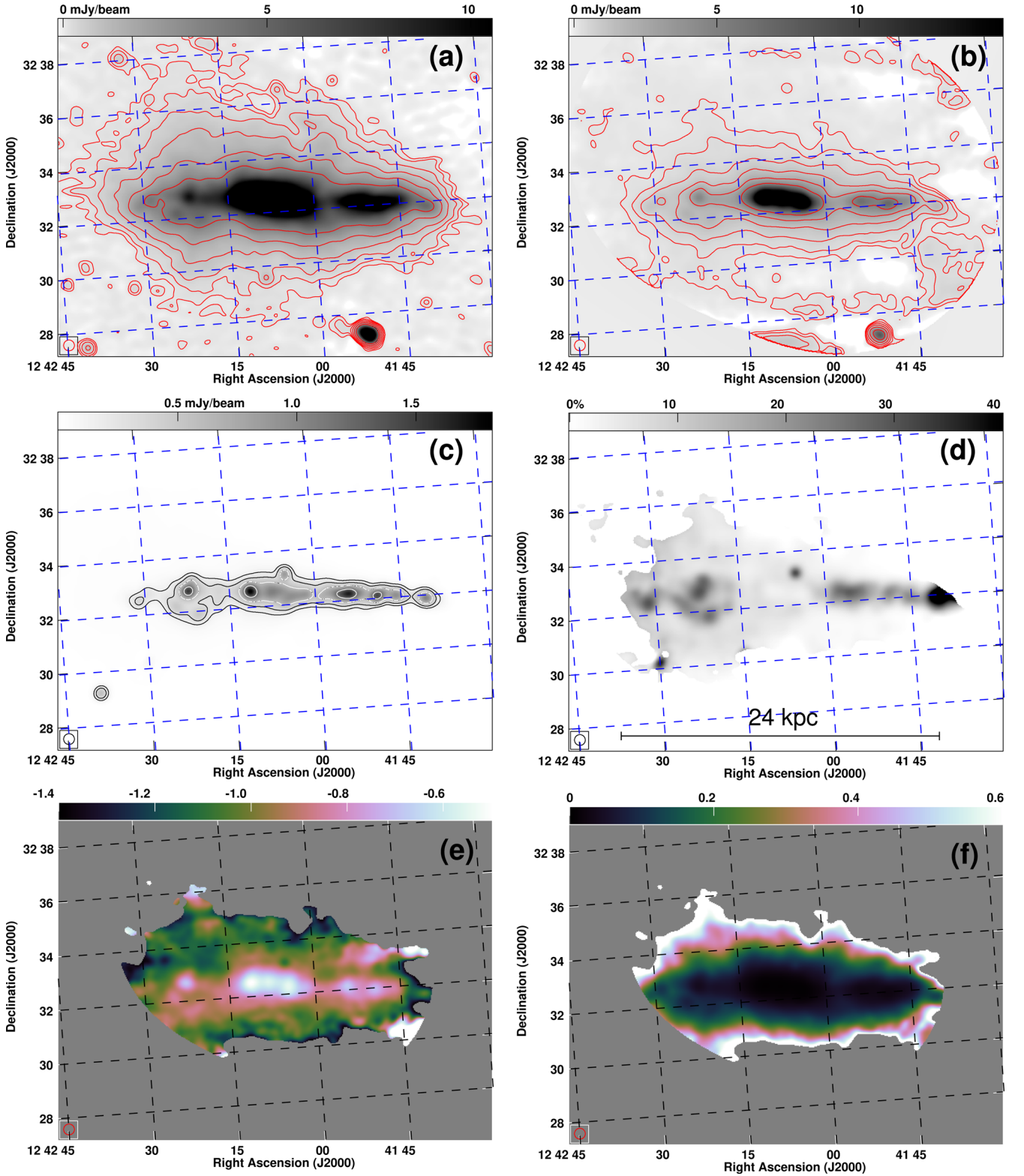
Figure 2. NGC 4631. (a) and (b) Radio continuum emission at 1.37 and 4.86 GHz, respectively. The high noise level near the edge of the 4.86-GHz map stems from the correction for the primary beam attenuation of the VLA. (c) The thermal radio continuum emission at 4.86 GHz. Contours in panels (a)–(c) are at (3, 6, 12, 24, 48, and 96) × σ, where σ is the rms map noise. In panel (c), the same contour levels as in panel (b) are used to ease the comparison. (d) Thermal fraction at 4.86 GHz, where the grey-scale ranges from 0 to 40 per cent. (e) Non-thermal radio spectral index between 1.37 and 4.86 GHz, where the colour scale ranges from −1.4 to −0.5. (f) Error of the non-thermal radio spectral index, where the colour scale ranges from 0 to 0.6. In all panels, the synthesized beam is shown in the bottom-left corner and the maps are rotated so that the major axis is horizontal.

Figure 3. Vertical profiles in NGC 4631. (a) Non-thermal radio continuum intensities at 1.37 and 4.86 GHz. We fitted a two-component exponential function (solid line) to the profiles. Black dashed lines show the effective beam, which is $I_{beam}(z) = \exp(-z^2/(2b^2))$ (see Section 3.3.1). (b) Non-thermal radio spectral index between 1.37 and 4.86 GHz. Lines show the best-fitting advection models, with an advection speed of 300 km s^{-1} in the northern halo (blue solid line) and 200 km s^{-1} in the southern halo (red dashed line). (c) Normalized non-thermal intensity model profile at 1.37 GHz, which is deconvolved from the synthesized beam. The red line shows the intensities of the best-fitting advection model. (d) Model of the magnetic field strength with uncertainties (blue shaded area). Distances $z > 0$ refer to the northern halo and distances $z < 0$ to the southern one. In panels (a)–(c), the size of the symbols is equivalent to the size or the error bars.

If there is no wind, the radio halo may be diffusion dominated. As HD16 showed, the vertical profile of the radio spectral index can be used in order to distinguish between advection and diffusion. Advection has spectral index profiles, which gradually steepen as a function of height. In contrast, diffusion leads to spectral index profiles that steepen only very little at small heights, but have steep cut-offs at large heights. This is caused by a steep cut-off of the CRE number density at large heights in the case of diffusion, which reflects the fact that the CREs cannot escape the galaxy. Thus, the vertical diffusion spectral index profiles have 'parabolic' shapes, which should distinguish them from the 'linear' advection profiles. In practice, it can, however, be difficult to allow for a distinction since the uncertainties of the radio spectral index are too large. Therefore, we fitted all our galaxies with both advection and diffusion models.

We find that only NGC 7462 can be fitted with a diffusion coefficient roughly in agreement with what we would expect, namely $D_0 \approx 3 \times 10^{28}$ cm^2 s^{-1}. All other galaxies required values in excess of this, with values between 1.2×10^{29} (NGC 55) and 4×10^{30} cm^2 s^{-1} (NGC 4666). There is no physical reason why the diffusion coefficient should deviate so much from the Milky Way

value, because the magnetic field structure is not too dissimilar.[8] Such high diffusion coefficients would also lead to the cosmic rays leaving the galaxy without interaction, so that they do not transfer energy and momentum to the ionized gas. This is at odds with cosmic ray-driven wind models, which now have become very popular (e.g. Breitschwerdt, McKenzie & Völk 1991; Everett et al. 2008; Samui, Subramanian & Srianand 2010; Salem & Bryan 2014). Their advantage over previous models is that they can explain the existence of winds in galaxies with $\Sigma_{SFR} \ll 10^{-1}$ M$_\odot$ yr^{-1} kpc^{-2}, where thermally driven winds suffer from too strong radiative cooling. Thus, we rule out models with $D_0 > 10^{29}$ cm^2 s^{-1} and assume that haloes are in this case advection dominated.

---

[8] The ratio of ordered (vertical to the line of sight) magnetic field strength to total magnetic field strength in late-type spiral galaxies is $B_{ord, \perp}/B_{tot} = 0.3$ with some fluctuations within the galaxies (maxima in the inter-arm regions, minima in the spiral arms; Fletcher 2010). This is similar to what has been found in radio haloes (see Section 3.1.3 for references). Hence, we expect similar diffusion coefficients to what is found in galactic discs.
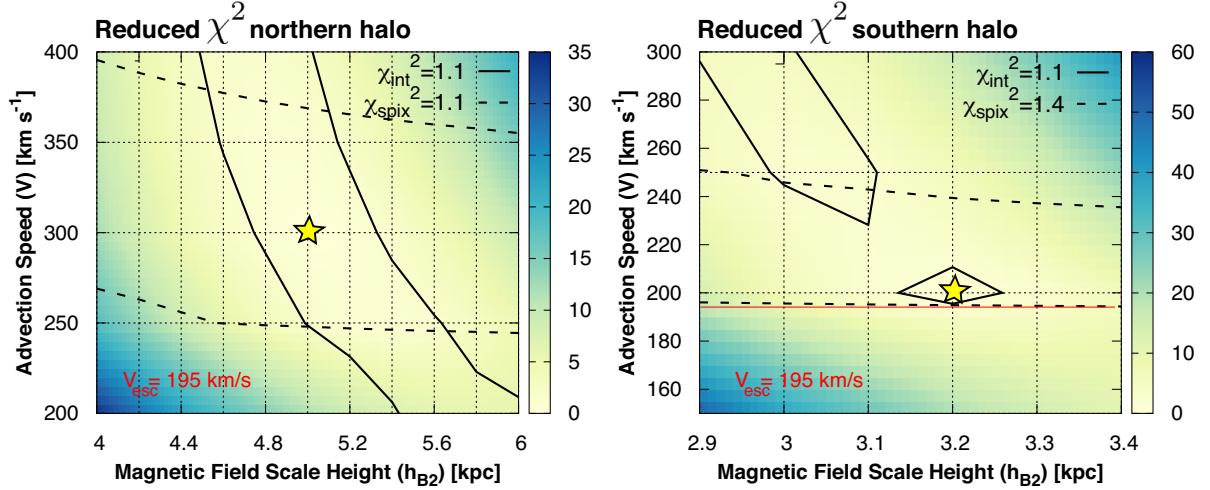
Figure 4. NGC 4631. Reduced χ^2 of the advection model fitting in the thick disc as a function of magnetic field scale height and the advection speed. The colour scale shows $\chi^2 = \chi_{int}^2 + \chi_{spix}^2$, where χ_{int}^2 refers to the model intensity profile (Fig. 3c) and χ_{spix}^2 refers to the spectral index profile (Fig. 3b). Solid lines show $\chi_{int,min}^2 + 1$ and dashed lines show $\chi_{spix,min}^2 + 1$. The best-fitting models (with uncertainties) lie in the intersection of the two contours and are marked by yellow stars. The left-hand panel is for the northern halo ($z > 0$) and the right one for the southern halo ($z < 0$). The red line shows the escape velocity near the mid-plane ($V_{esc} = \sqrt{2} \times V_{rot}$).

Table 7. Non-thermal intensity scale height z_0 at L and C band, advection speed V, diffusion coefficient D_0 ($D = D_0 E_{GeV}^{0.5}$), and magnetic field scale height of the thin (h_{B1}) and thick disc (h_{B2}) in the northern (N) and southern (S) halo.

Galaxy	z_0 (L/N)[a] (kpc)	z_0 (C/N)[b] (kpc)	z_0 (L/S)[c] (kpc)	z_0 (C/S)[d] (kpc)	h_{B1} (N)[e] (kpc)	h_{B1} (S)[f] (kpc)	h_{B2} (N)[g] (kpc)	h_{B2} (S)[h] (kpc)	V (N)[i] (km s^{-1})	V (S)[j] (km s^{-1})
NGC 55	2.03 ± 1.46	1.72 ± 0.22	1.06 ± 0.14	2.01 ± 0.71	0.3 ± 0.1	0.2 ± 0.1	$4.0^{++2.0}_{-1.2}$	$2.5^{+0.8}_{-0.7}$	150^{++200}_{--100}	100^{+80}_{-10}
NGC 253	1.26 ± 0.07	1.14 ± 0.04	1.33 ± 0.04	1.28 ± 0.02	N/A	N/A	$2.8^{+0.2}_{-0.7}$	$3.0^{+0.1}_{-0.5}$	400^{+200}_{-20}	500^{++400}_{-120}
NGC 891	1.33 ± 0.02	1.30 ± 0.02	1.25 ± 0.01	1.24 ± 0.03	0.1 ± 0.1	0.2 ± 0.1	$3.0^{+0.2}_{-0.2}$	$2.5^{+0.2}_{-0.2}$	600^{++600}_{-200}	600^{++600}_{-200}
NGC 3044	3.64 ± 0.95	1.47 ± 0.26	1.30 ± 0.08	1.15 ± 0.14	0.5 ± 0.1	0.5 ± 0.1	$4.5^{++4.5}_{-1.7}$	$3.0^{+0.7}_{-0.6}$	200^{++200}_{-50}	200^{+200}_{-50}
NGC 3079	5.14 ± 8.86	1.00 ± 0.19	3.41 ± 0.63	1.54 ± 0.10	1.2 ± 0.1	1.0 ± 0.1	$4.5^{+7.5}_{-2.0}$	$8.0^{+7.0}_{-3.0}$	300^{+80}_{-40}	400^{+80}_{-80}
NGC 3628	1.23 ± 0.05	1.16 ± 0.04	N/A	0.87 ± 0.02	0.1 ± 0.1	0.1 ± 0.1	$2.6^{+0.3}_{-0.3}$	$2.0^{+0.1}_{-0.3}$	250^{+250}_{-50}	250^{++400}_{-50}
NGC 4565	1.90 ± 0.10	1.63 ± 0.07	3.11 ± 0.66	1.75 ± 0.10	N/A	0.8 ± 0.1	$3.5^{+1.1}_{-0.5}$	$4.0^{+0.2}_{-0.7}$	500^{++300}_{-220}	250^{+150}_{-20}
NGC 4631	2.24 ± 0.07	1.70 ± 0.05	1.47 ± 0.02	1.13 ± 0.02	0.6 ± 0.1	0.4 ± 0.1	$5.0^{+0.6}_{-0.5}$	$3.2^{+0.1}_{-0.2}$	300^{+80}_{-50}	200^{+50}_{-20}
NGC 4666	1.51 ± 0.05	1.54 ± 0.03	2.01 ± 0.08	1.70 ± 0.11	0.5 ± 0.1	0.5 ± 0.1	$3.0^{+0.3}_{-0.3}$	$4.0^{+0.4}_{-0.5}$	700^{++200}_{-100}	500^{+80}_{-70}
NGC 5775	2.72 ± 0.12	1.27 ± 0.06	1.91 ± 0.12	2.03 ± 0.80	1.0 ± 0.1	0.4 ± 0.1	$7.0^{+1.5}_{-1.0}$	$4.0^{++2.0}_{-0.8}$	400^{+100}_{-50}	450^{++100}_{--150}
NGC 7090	2.07 ± 0.18	1.96 ± 0.50	1.53 ± 0.39	1.14 ± 0.44	0.6 ± 0.1	0.4 ± 0.1	$5.5^{+1.0}_{-1.2}$	$4.5^{+3.5}_{-2.7}$	200^{+310}_{-10}	300^{++300}_{-120}
NGC 7462	1.62 ± 0.15	1.38 ± 0.03	1.50 ± 0.03	1.46 ± 0.01	N/A	N/A	$3.0^{+1.0}_{-0.2}$	$3.5^{+0.7}_{-0.5}$	<80	<100

Galaxy							h_{B2} (N)[g] (kpc)	h_{B2} (S)[h] (kpc)	D_0 (N)[i]	D_0 (S)[j]
									(10^{28} cm^2 s^{-1})	
NGC 7462							$3.0^{+1.0}_{-0.2}$	$3.5^{+0.7}_{-0.5}$	$2.2^{+0.4}_{-0.4}$	$2.6^{+0.1}_{-0.6}$

Notes. Values with '++' or '−−' have no upper or lower limits. Where no upper limit for V was measured, we use $I_{int} \propto B^{1-\alpha_{nt}}$ for freely escaping CREs to estimate the lower limit of h_{B2}.
[a]Non-thermal exponential (Gaussian for NGC 7462) intensity scale height at L band in the thick disc in the northern halo.
[b]Non-thermal exponential (Gaussian for NGC 7462) intensity scale height at C band in the thick disc in the northern halo.
[c]Non-thermal exponential (Gaussian for NGC 7462) intensity scale height at L band in the thick disc in the southern halo.
[d]Non-thermal exponential (Gaussian for NGC 7462) intensity scale height at C band in the thick disc in the southern halo.
[e]Magnetic field scale height in the thin disc in the northern halo. NGC 253, 4565, and 7462 have only a thick disc in the northern halo.
[f]Magnetic field scale height in the thin disc in the southern halo. NGC 253 and 7462 have only a thick disc in the southern halo.
[g]Magnetic field scale height in the thick disc in the northern halo.
[h]Magnetic field scale height in the thick disc in the southern halo.
[i]Advection speed (diffusion coefficient for NGC 7462) in the northern halo.
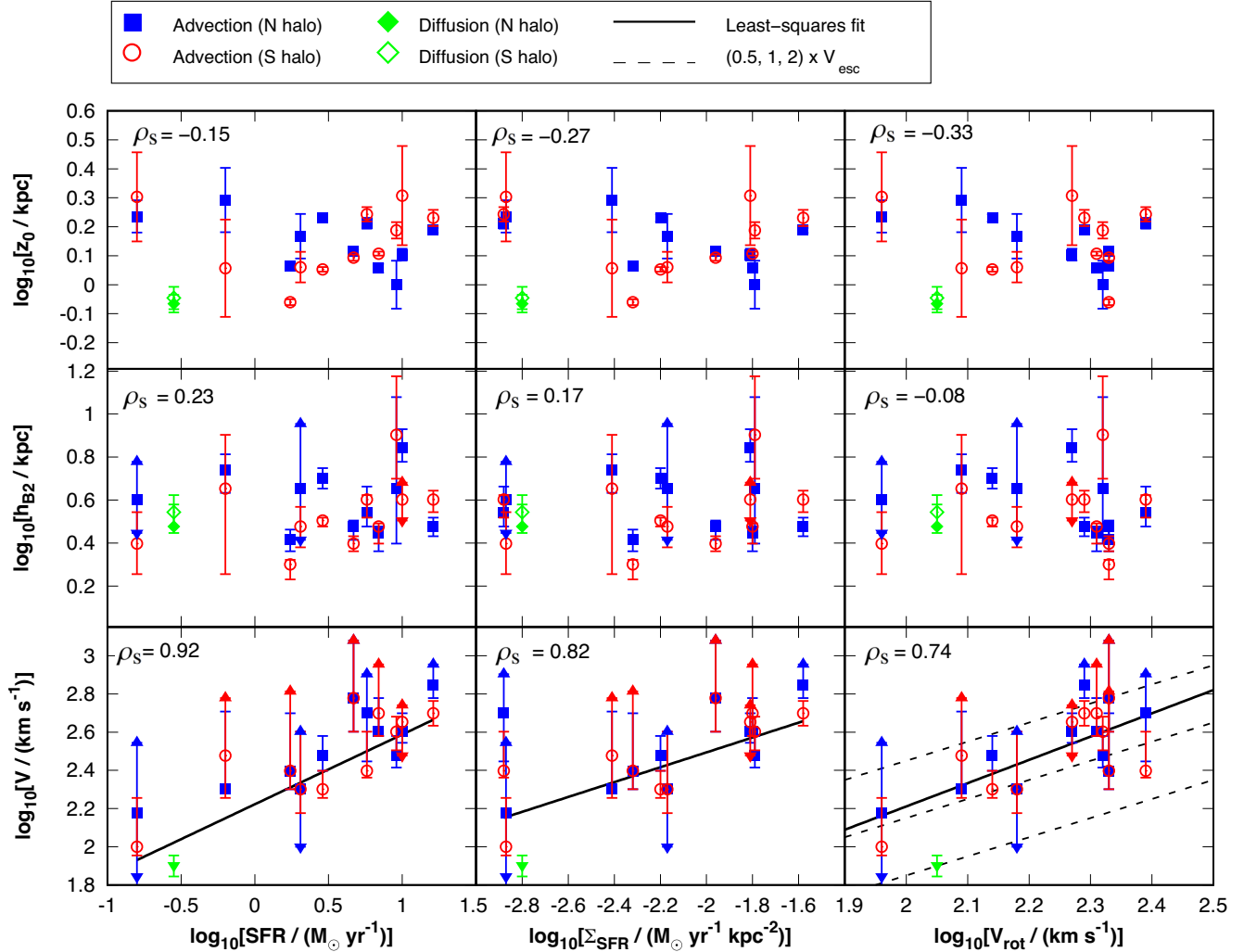[j]Advection speed (diffusion coefficient for NGC 7462) in the southern halo.

Figure 5. Parameter studies in log–log diagrams as a function of SFR, SFR surface density (Σ_{SFR}), and rotation speed V_{rot}. Top panels: non-thermal intensity scale height (z_0) at 5 GHz (8.5 GHz for NGC 5775) of the thick radio disc. Middle panels: magnetic field scale height (h_{B2}) of the thick radio disc. Bottom panels: advection speed (V), where solid lines show least-squares fits. In the bottom-right panel, the dashed lines show $(0.5, 1, 2) \times V_{esc}$. In each panel, we also present Spearman's rank correlation coefficient, ρ_s, which we derived from values that have both upper and lower limits.

4.2 Non-thermal intensity scale heights

We find that the vertical non-thermal intensity profiles in seven out of the 12 sample galaxies are better fitted by exponential rather than Gaussian functions, where $\chi^2_{exp} - \chi^2_{Gauss} \leq -1$ (NGC 55, 891, 3044, 3079, 3628, 4631, and 5775; the reduced χ^2 values are the average of the northern and southern halo at both frequencies). In three galaxies, the fits are of equivalent quality, where $-1 < \chi^2_{exp} - \chi^2_{Gauss} < 1$ (NGC 253, 4565, and 7090). Only in one galaxy, the Gaussian fits significantly better than the exponential function, where $\chi^2_{exp} - \chi^2_{Gauss} \geq 1$ (NGC 7462). In 10 out of the 11 exponential haloes (including the seven better and the three equivalent fits), we also detect a thin disc component. Only in NGC 4565, this is not the case, which we believe is due to a combination of low spatial resolution and disc intensity (NGC 4565 has the lowest average surface intensity). We detect a thick disc in the Magellanic-type galaxy NGC 55 (Appendix D), the first report of a radio halo in this galaxy.

Averaged across the sample, the exponential scale height of the thin disc is 0.41 ± 0.21 kpc at 1.4 GHz and 0.25 ± 0.13 kpc at 5 GHz. The scale height of the thick disc is 1.33 ± 1.25 kpc at

1.4 GHz and 1.22 ± 0.43 kpc at 5 GHz; these values are in excellent agreement with those of Krause et al. (2017). We found a large variety of scale heights at 1.4 GHz ranging between 1.2 and 2.7 kpc (excluding values with fractional errors larger than 10 per cent). At 5 GHz, the scale heights of the thick disc vary between 0.9 and 2.0 kpc. In NGC 7462, we find only a thick Gaussian disc with a scale height of ≈ 1.5 kpc at both 1.4 and 5 GHz.

In Fig. 5, we show the dependence of the 5-GHz intensity scale heights as a function of the SFR, Σ_{SFR}, and V_{rot}. These are log–log diagrams so that we can fit linear functions to them, which are representative of power laws. We find no correlation between the intensity scale height and either parameter (Spearman's rank correlation coefficient $|\rho_s| \leq 0.33$). Full results of the scale height fitting are presented in Appendix B.

4.3 Non-thermal radio spectral indices

We find that in those seven galaxies that have both a thin and a thick disc, the vertical non-thermal radio spectral index profile shows the thin and the thick disc clearly separated as well (NGC

55, 891, 3044, 3628, 4631, 5775, and 7090). The exceptions are NGC 253, 4565, and 4666, where the thin and the thick disc are difficult to separate in the intensity profiles. This is caused by either low inclination angles ($<79°$ in NGC 253 and 4666) or low spatial resolution (2.1 kpc in NGC 4565). In NGC 3079, we can separate the thin and the thick disc in the intensity profile, but the slope of the spectral index profile in the thick disc is so high that there is no visible transition from the thin to the thick disc. Even though we have masked the nuclear outflow, it is possible that additional diffuse emission associated with it can contaminate our radio continuum emission. Since this is more pronounced at L band, where the scale heights in the thick radio discs are the largest in our sample, old CREs, possibly stemming from an earlier episode of AGN activity, could be responsible for this emission. Such emission can also be explained as the result of jet interactions with clumpy media (Middelberg et al. 2007), which can contaminate the radio emission around the thin/thick disc transition. In all galaxies, the non-thermal radio spectral index in the thick disc varies between -1.4 and -1.0, showing that spectral ageing of the CREs plays an important role in the halo.

The integrated non-thermal radio spectral indices range from -1.3 (NGC 7462) to -0.6 (NGC 55). The significance of the integrated non-thermal spectral index is that we can infer which energy losses of the CREs are dominating. If synchrotron and IC radiation losses are important, the CRE spectrum is $N(E, z) \propto E^{-\gamma_{inj}-1}$. If, on the other hand, adiabatic losses dominate or the CREs escape freely, the CRE spectrum is unchanged from the injection spectrum with $N(E, z) \propto E^{-\gamma_{inj}}$ (Lisenfeld & Völk 2000; Longair 2011). In case radiation losses are important, a galaxy is referred to as an *electron calorimeter*, where the CREs are losing their energy before they can escape through radiation and ionization losses (Yoast-Hull et al. 2013).

This shows that NGC 55 is not an electron calorimeter, whereas NGC 7462 is one. NGC 55 is a Magellanic-type dwarf irregular galaxy and possibly has a strong wind, similar to the starburst dwarf irregular galaxy IC 10 (Chyży et al. 2016). On the other hand, NGC 7462 is diffusion dominated (no wind) and all the CREs are confined in the halo, leading to high CRE radiation losses. Our finding that galaxies have galactic winds means that galaxies are in general not electron calorimeters. This has some consequences for the radio continuum–SFR relation and its close corollary the radio continuum–far-infrared relation, which we discuss in Section 5.2.

4.4 Magnetic field scale heights

In the thin disc, magnetic field scale heights range from 0.1 kpc in NGC 3628 to 1.2 kpc in NGC 3079. Averaged across the sample, the magnetic field scale height in the thin disc is 0.50 ± 0.32 kpc (assuming an error of 0.1 kpc for each measurement). In the thick disc, we find scale heights between 2 kpc in NGC 3628 and 8 kpc in NGC 3079. In Fig. 5, we show that the magnetic field scale height of the thick disc does not depend on either SFR, Σ_{SFR}, or V_{rot}. The magnetic field in the halo must be regulated by something else than the wind driven by the star formation in the disc. Maybe the geometry plays a role, as for instance predicted by the flux tube model used in the aforementioned 1D cosmic ray-driven wind models. The large scale heights in NGC 3079 can possibly be explained by the strong interaction of this galaxy with nearby group members (Shafi et al. 2015). Tidal interaction can 'puff' up the thin and the thick discs by inflating the warm neutral medium, which in our picture results in a larger magnetic field scale height. Alternatively, the prominent starburst/AGN-driven nuclear outflow

advects cosmic rays and magnetic fields, so that the magnetic field extends further into the halo (Cecil et al. 2001; Middelberg et al. 2007).

Averaged across our sample, the magnetic field scale height in the thick disc is 3.0 ± 1.7 kpc. Compared with the magnetic field scale height predicted by energy equipartition, $h_B \approx 4 \cdot z_0$ (where z_0 is the 5-GHz intensity scale height) for $\alpha_{nt} \approx -1$, the magnetic field scale height in the thick disc is 35 per cent lower. This is because the vertical decrease of the CRE number density is smaller than that of the magnetic field energy density (fig. 10 in HD16).

4.5 Advection speeds

The advection speeds range from 100 km s^{-1} in NGC 55 to 700 km s^{-1} in NGC 4666. The advection speeds rise as $V \propto$ SFR$^{0.36\pm0.06}$ and $V \propto \Sigma_{SFR}^{0.39\pm0.09}$ as shown in Fig. 5. We found Spearman's rank correlation coefficients of $\rho_s = 0.92$ and 0.82, respectively; for this we used a least-squares fitting routine in the log–log diagram, taking only data points with both upper and lower limits into account (that have no arrows in Fig. 5). These correlations are robust with respect to performing the 'jackknife' test, where we leave out NGC 55, the galaxy with the lowest SFR. We find another possible correlation with V_{rot}, which is, however, not robust to the jackknife test. We need more observations of dwarf irregular galaxies to measure winds in them. A correlation between advection speed and SFR has been suggested earlier based on the observation that the 5-GHz radio continuum scale height is almost constant and does not depend on the magnetic field strength in the mid-plane (Krause 2015). If one assumes that the scale height is a function of the CRE lifetime, neglecting the influence of the magnetic field, then scale height scales as $\propto B_0^{-1.5}$, where it is also assumed that synchrotron losses are dominating over IC losses (Appendix A). If one now uses that the magnetic field strength scales as $B_0 \propto$ SFR$^{0.3}$ (e.g. Heesen et al. 2014), one can conclude that the scale height scales as $\propto$ SFR$^{-0.5}$. Hence, in order to have a constant scale height, the advection speed has to scale as $V \propto$ SFR$^{0.5}$ (Krause 2015). In reality, the magnetic field scale height also plays a role, so that the scaling is somewhat less with the SFR, but the general idea is a valid one.

The advection speeds lie within the range $0.5 \leq V/V_{esc} \leq 2$ (including the uncertainties), where $V_{esc} = \sqrt{2} \times V_{rot}$ is the escape velocity near the mid-plane (further away from the disc, in the dark matter halo, the escape velocity is higher). In NGC 7462, where diffusion dominates, we can calculate an upper limit for the advection speed, by comparing how much advection can contribute at most. This can be done either analytically using equation (7), inserting $s_\star = 2.5$ kpc, the CRE scale height in NGC 7462 (fig. 10 in HD16), or numerically by comparing profiles of the CRE number density. Both ways give a similar result, namely that the upper limit for the advection speed in NGC 7462 is between 80 and 100 km s^{-1}.

Are we tracing really disc winds, or are the radio haloes only extensions to the nuclear outflows seen in galaxies with nuclear starbursts or AGNs? A case in point is NGC 3079, a galaxy with a low-luminosity AGN. On the northern side of the galaxy, a nuclear outflow is detected with an outflow speed of the warm ionized gas of up to ≈ 1000 km s^{-1} (Cecil et al. 2001). There is also a nuclear outflow on the southern side, which can be seen only in the radio continuum due to absorption by dust of the optical emission. A similar outflow, albeit less prominent in the radio continuum, can be seen in the nuclear region of NGC 253 (Heesen et al. 2011; Westmoquette et al. 2011). Here, the nuclear outflow speed is of the order of ≈ 300 km s^{-1}, traced by the Doppler shift of the warm

ionized gas. The other galaxies in our sample have not been studied in detail with regard to their nuclear outflows, although the study by Ho et al. (1997) of the [N II] emission line offers some clues. Our samples have in common NGC 891, 3079, 3628, 4565, 4631, and 5775. Their line widths are all smaller than our advection speeds, with the exception of NGC 3079. In NGC 891, 3628, and 5775, the line-width equivalent velocity is less than 50 per cent of our advection speed. Studying nuclear outflows and determining their kinematics is very challenging and is usually based on the presence of unusually broad or shifted lines (or lines with excess wing emission). Even when such features are identified, it is extremely difficult to distinguish between rotation, inflow, or outflow (often outflows are inferred from the presence of velocities exceeding the escape velocity of the host galaxy). Hence, it is not possible to compare the properties of nuclear outflows and disc winds in detail for our sample.

5 DISCUSSION

5.1 Cosmic ray-driven winds

Our result of increasing advection speeds as a function of the SFR is also observed in studies of other low-redshift galaxies, where the wind speed of either the warm ionized gas (e.g. Arribas et al. 2014; Heckman et al. 2015; Heckman & Borthakur 2016) or the neutral gas (e.g. Martin 2005; Rupke, Veilleux & Sanders 2005) is measured. This can be explained by a star formation-driven wind due to a combination of a hot wind fluid driven by the thermalized ejecta of massive stars and radiation pressure. Another explanation is cosmic ray-driven winds, where the cosmic ray pressure (via Alfvén waves) in conjunction with the pressure of the thermal gas pushes the material outwards. Hybrid forms of winds are also possible. Cosmic ray-driven winds are predominant for galaxies with low Σ_{SFR}, where the pressure of the thermal gas alone is insufficient to launch a wind (Everett et al. 2008). The influence of the cosmic ray pressure can be tested with our observations: the magnetic field strength in galaxies scales as $B \propto SFR^{0.30\pm0.02}$ (Heesen et al. 2014), similar to the relation of the advection speeds, which is $V \propto SFR^{0.36\pm0.06}$. Hence, the magnetic field strength and the advection velocity are nearly proportional to each other. This also means that $V^2 \propto B^2$, so that the kinetic energy density of the wind $U_{kin} = (1/2)\rho V^2$ is proportional to the magnetic energy density $U_B = B^2/(8\pi)$; here, ρ is the density of the hot ionized gas. This may tell us that the wind is driven by cosmic rays, which are roughly in equipartition with the magnetic field.

Another important result is the remarkable agreement between advection speeds and escape velocities. Again, this can be explained by cosmic ray-driven winds. Initially, the wind speed is below the sound speed of the combined thermal and cosmic ray gas (the so-called compound sound speed), but the flow accelerates in the halo where it goes through the critical point (Mach number $M = 1$) at a distance of a few kpc away from the disc. Eventually, the wind accelerates further to reach an asymptotic velocity of a few times the escape velocity (Breitschwerdt et al. 1991; Everett et al. 2008). Wind speeds of the order of the escape velocity are also predicted for pressure-driven galactic winds without the contribution from cosmic rays (Murray, Quataert & Thompson 2005; Heckman et al. 2015; Heckman & Borthakur 2016). The accelerating force in momentum-driven winds is a combination of radiation pressure, ram pressure from galactic winds, and non-thermal pressure due to

magnetic fields and cosmic rays.[9] It is an intriguing possibility that galactic winds are driven by the combined pressure supplied by star formation (via SN ejecta and stellar winds) and cosmic rays.

Within the critical point, the compound sound speed can be approximated by (Breitschwerdt et al. 1991)

$$c_{comp}^2 \approx \frac{1}{2} g_{eff} \frac{Z_0^2}{z_c},$$ (8)

where g_{eff} is the gravitational acceleration in the halo, Z_0 is the height where the flow becomes spherical, and z_c is the height of the critical point. The gravitational acceleration can be approximated by $g_{eff} \approx V_{rot}^2/r_\star$ because the flow emanates as a disc wind from radii with active star formation ($r \leq r_\star$). We do not know where the critical point lies, but it must be of the order of the magnetic field scale height since our outflow speeds are already exceeding the escape velocity. Hence, setting $z_c \approx h_B$, we find for the compound sound speed

$$c_{comp} = V_{rot} \cdot \frac{Z_0}{\sqrt{2r_\star \cdot h_B}}.$$ (9)

With $r_\star \approx 10\,kpc$, $Z_0 \approx 15\,kpc$, and $h_B \approx 3\,kpc$, we find $c_{comp} \approx 2 \cdot V_{rot}$, in good agreement with our advection speeds. While the exact numerical value of equation (9) is uncertain, the prediction is that the advection speeds of cosmic ray-driven winds scale with the rotation speeds and are similar to the escape velocities.

The particular value of our radio continuum observations lies in the fact that we can measure wind speeds for galaxies with $\Sigma_{SFR} < 0.3 \times 10^{-1}\,M_\odot\,yr^{-1}\,kpc^{-2}$, whereas conventional absorption and emission line studies have so far focused on galaxies exceeding this limit. All of our sample galaxies fulfil $\Sigma_{SFR} > 10^{-3}\,M_\odot\,yr^{-1}\,kpc^{-2}$, for which Rossa & Dettmar (2003a) detect extra-planar diffuse ionized gas (eDIG). Only in NGC 7462, which has $\Sigma_{SFR} = 1.6 \times 10^{-3}\,M_\odot\,yr^{-1}\,kpc^{-2}$, we find a diffusion-dominated halo. This galaxy is only marginally above the Σ_{SFR} threshold. This leaves the possibility that galaxies with no eDIG are diffusion dominated and have no outflows in them, whereas galaxies with eDIG are advection dominated and have outflows. We need to extend this kind of study to galaxies with lower Σ_{SFR} to confirm this theory.

5.2 Radio–SFR relation

Radio continuum emission in galaxies emerges from two distinct processes: thermal free–free (bremsstrahlung) and non-thermal (synchrotron) radiation. Both are related to the formation of massive stars. UV radiation from massive stars ionizes the ISM, which gives rise to the free–free emission. The explanation of the non-thermal radio continuum emission (which dominates at frequencies below ≈30 GHz) is more involved: massive stars end their lives as SNe. When the blast wave of the explosion reaches the ISM, strong shocks are formed, which accelerate protons, nuclei, and electrons. The CREs spiral around the interstellar magnetic field lines, thereby emitting highly linearly polarized synchrotron emission. The relation between the radio continuum luminosity of a galaxy and its SFR (in the following, the radio–SFR relation) is due to the interplay of star formation, CREs, and magnetic fields.

---

[9] Pressure-driven winds are also sometimes referred to as momentum-driven winds in the literature. In our case, the cosmic ray-driven wind implicitly means a momentum-driven wind since the cooling of the thermal gas is so strong that the influence of the cosmic ray pressure becomes important.

The radio–SFR relation is very tight, as Heesen et al. (2014) have shown: using the relation of Condon (1992), and converting 1.4-GHz radio luminosities into radio-derived SFRs, they found agreement within 50 per cent with state-of-the-art star formation tracers, such as FUV, Hα, and mid- or far-infrared emission. An even better agreement can be achieved if the radio spectrum is integrated over a wide frequency range ('bolometric radio luminosity'; Tabatabaei et al. 2017). Moreover, these authors found that the radio luminosity is a non-linear function of the SFR, as predicted by the model of Niklas & Beck (1997) as detailed below. In radio haloes, the spatially resolved radio–SFR relation is super-linear as well if we take the λ850-μm far-infrared emission as a proxy for the SFR (Irwin et al. 2013).

It has been realized early on (Condon 1992) for the non-thermal radio continuum emission to be related to the SFR that (i) the CREs have either to emit all their energy within a galaxy, so that the galaxy constitutes an electron calorimeter; (ii) or the cosmic rays have to be in energy equipartition with the magnetic field *and* there is a magnetic field–SFR or magnetic field–gas relation (Niklas & Beck 1997). Model (i) predicts a linear non-thermal radio–SFR relation, and model (ii) a non-linear one. Present-day observations of spiral galaxies favour model (ii), which is expected since galaxies in general are not electron calorimeters. Electron calorimetry might hold at best in starburst galaxies, but almost certainly not in low-mass dwarf irregular galaxies, which lose a large fraction of their CREs in galactic winds and outflows (e.g. Chyży et al. 2016).

We can now confirm that even normal massive late-type spiral galaxies do have such outflows, which can reasonably explain why energy equipartition is found in them. In this picture, the SFR determines the magnetic field strength. The model by Niklas & Beck (1997) uses the elegant way of assuming a magnetic field–gas relation (the turbulent energy density of the magnetic field is equivalent to the magnetic field energy density), from which the magnetic field–SFR relation is the result of the Kennicutt–Schmidt relation. Then, a galaxy can only store as many cosmic rays as the magnetic field can contain. If the cosmic ray pressure becomes too high, the buoyant cosmic ray gas will escape together with the magnetic field from the galaxy. Cosmic ray-driven winds serve thus as a 'pressure valve' that allows overabundant cosmic rays to escape and thus preserve the energy equipartition with the magnetic field.

5.3 Magnetic field uncertainties

The largest source of uncertainty in our study stems from the estimate of the magnetic field strength assuming energy equipartition. This assumption is supported by the observed relation between radio continuum luminosity and SFR (Section 5.2). Non-calorimetric models require energy equipartition, while calorimetric models are not in good agreement with the observations (Niklas & Beck 1997; Heesen et al. 2014; Li et al. 2016). Nevertheless, it is interesting to note what happens when we increase or decrease the magnetic field strength by a factor of 2. Because the typical halo magnetic field strength is $B_{halo} \approx 3\,\mu$G, the IC losses in the radiation field of the CMB become comparable to the synchrotron losses of the CREs (the CMB equivalent magnetic field strength is $B_{CMB} = 3.2\,\mu$G). The CRE lifetime, as determined by synchrotron and IC radiation losses, can be expressed by (HD16)

$$t_{rad} = 34.2 \left(\frac{\nu}{1\,\text{GHz}}\right)^{-0.5} \left(\frac{B}{10\,\mu\text{G}}\right)^{-1.5} \left(1 + \frac{U_{rad}}{U_B}\right)^{-1} \text{Myr}.$$

(10)

If we now decrease and increase the magnetic field strength by a factor of 2, we have $B_{halo,-} = 1.5\,\mu$G, $B_{halo} = 3.0\,\mu$G, and $B_{halo,+} = 6.9\,\mu$G. Inserting this into equation (10) and neglecting the radiation energy density from the star-forming disc, so that $U_{rad} = U_{CMB} = (3.2\,\mu\text{G})^2/(8\pi)$, we find $t_{rad,-} = 90$, $t_{rad} = 75$, and $t_{rad,+} = 48$ Myr. Hence, for the lower magnetic field strength, the advection speed increases by 20 per cent, whereas for the higher magnetic field strength, the advection speed increases by 60 per cent. In summary, the uncertainty of the magnetic field strength provides *lower* limits for the advection speeds. Even if the magnetic field strength is in reality a factor of 2 lower, the advection speed decreases only little since the IC losses are compensating for the smaller synchrotron losses.

6 CONCLUSIONS

In this paper, we present radio continuum observations of 12 nearby ($D = 2$–27 Mpc) edge-on galaxies at two different frequencies, namely at 1.4 and 5 GHz (one galaxy at 8.5 GHz instead of 5 GHz). Our sample includes 11 late-type spiral (Sb or Sc) galaxies and one Magellanic-type barred galaxy (SBm), which are all highly inclined ($i \geq 76°$). The angular resolution of our maps varies between 8.25 and 41.1 arcsec, which corresponds to spatial resolutions at the distances of the galaxies between 0.4 and 2.1 kpc. We subtracted the thermal radio continuum emission using Balmer Hα maps (or *Spitzer* 24-μm maps, scaled to Hα) to study the non-thermal radio continuum emission in the halo (where internal absorption by dust can be neglected). We fitted the vertical intensity profiles with exponential and Gaussian functions, correcting for the effective beam (the combined effect of angular resolution and projection). The intensity model profiles and the spectral index profiles in the halo ($|z| \gtrsim 1$ kpc) were then fitted with 1D cosmic ray transport models from the software SPINNAKER. In this way, we simultaneously measured CRE advection speeds (or diffusion coefficients) and magnetic field scale heights. These are our main conclusions.

(i) We discover a previously unknown radio halo in the Magellanic-type galaxy NGC 55 (see Appendix D). This galaxy is hence another example of a dwarf irregular galaxy with a non-thermal outflow.

(ii) In seven out of 12 galaxies, we find exponential vertical intensity profiles and only in one galaxy we find a Gaussian profile. The profiles in the remaining galaxies can be equally well described by either an exponential or Gaussian distribution. We conclude that vertical intensity profiles in the thick radio discs are predominantly exponential.

(iii) In 11 out of 12 galaxies, we find a thin disc in addition to a thick disc. Averaged across the sample, the thin disc has an exponential scale height of 0.41 ± 0.21 kpc at 1.4 GHz and 0.25 ± 0.13 kpc at 5 GHz. The thick disc has an exponential scale height of 1.33 ± 1.25 kpc at 1.4 GHz and 1.22 ± 0.43 kpc at 5 GHz.

(iv) The magnetic field in the thin disc has a scale height of 0.50 ± 0.32 kpc. This is in approximate agreement with the expected value if the magnetic field is in pressure equilibrium with the warm neutral medium (H I disc).

(v) The vertical spectral index profiles show a clear separation between the thin and the thick disc in those cases where we see the separation also in the intensities ($i > 85°$, resolution <1 kpc). The spectral index profiles at $|z| \gtrsim 1$ kpc are linear as expected for cosmic ray advection. Only NGC 7462 shows the parabolic shape expected for diffusion. The spectral index separation shows two different CRE populations in the disc and halo. If superbubble

breakout is responsible for the separation, we would expect the transition to be happening at 0.5–1.5 kpc (three times the H I scale height).

(vi) The magnetic field scale height in the thick disc across our sample is 3.0 ± 1.7 kpc. In individual galaxies, it is not correlated with either SFR, Σ_{SFR}, or V_{rot}.

(vii) In 11 out of 12 galaxies, we find advection-dominated haloes. The advection speeds correlate as $V \propto SFR^{0.36\pm0.06}$ and $V \propto \Sigma_{SFR}^{0.39\pm0.09}$ and agree remarkably well with the escape velocity ($0.5 \leq V/V_{esc} \leq 2$). The scaling relations and the good agreement with the escape velocities can be explained by cosmic ray-driven winds, with the pressure supplied by star formation (via SN ejecta and stellar winds) and/or by cosmic rays (via Alfvén waves).

(viii) Radio haloes show the existence of disc winds that extend over the star-forming disc with an extension of several kpc at least. Cosmic rays are important to launch these winds, because averaged over the full extent of the disc, the Σ_{SFR} is low. In our sample, $10^{-3} \leq \Sigma_{SFR}/(M_\odot\ yr^{-1}\ kpc^{-2}) \leq 10^{-1}$, where we detect advective haloes in 11 out of 12 galaxies. The transition from diffusion- to advection-dominated haloes possibly happens at $\Sigma_{SFR} = 10^{-3}\ M_\odot\ yr^{-1}\ kpc^{-2}$, above which galaxies have winds, in agreement with the detection of eDIG in their haloes.

Our study demonstrates the usefulness of radio continuum observations to study galactic winds, complementary to spectroscopic studies of optical and FUV emission and absorption lines. As a next step, it would be desirable to repeat this kind of analysis for a larger sample of late-type spiral galaxies such as from the CHANG-ES survey (Irwin et al. 2012; Wiegert et al. 2015) and to include dwarf irregular galaxies such as from the LITTLE THINGS survey (Heesen et al. 2011; Hunter et al. 2012). Furthermore, low-frequency radio continuum observations with LOFAR (van Haarlem et al. 2013) will allow us to trace the oldest CREs far away from the galactic disc, of which early results show a prominent radio halo in NGC 5775 (Heald, Williams & Sridhar 2016).

REFERENCES

Adebahr B., Krause M., Klein U., Weżgowiec M., Bomans D. J., Dettmar R.-J., 2013, A&A, 555, A23

Arribas S., Colina L., Bellocchi E., Maiolino R., Villar-Martín M., 2014, A&A, 568, A14

Baars J. W. M., Genzel R., Pauliny-Toth I. I. K., Witzel A., 1977, A&A, 61, 99

Bagetakos I., Brinks E., Walter F., de Blok W. J. G., Usero A., Leroy A. K., Rich J. W., Kennicutt R. C., Jr, 2011, AJ, 141, 23

Basu A., Beck R., Schmidt P., Roy S., 2015, MNRAS, 449, 3879

Bauer M., Pietsch W., Trinchieri G., Breitschwerdt D., Ehle M., Freyberg M. J., Read A. M., 2008, A&A, 489, 1029

Beck R., 2016, A&AR, 24, 4

Beck R., Krause M., 2005, Astron. Nachr., 326, 414

Becker R. H., White R. L., Edwards A. L., 1991, ApJS, 75, 1

Bell A. R., 1978, MNRAS, 182, 147

Bendo G. J., Galliano F., Madden S. C., 2012, MNRAS, 423, 197

Berkhuijsen E. M., Beck R., Tabatabaei F. S., 2013, MNRAS, 435, 1598

Braun R., Oosterloo T. A., Morganti R., Klein U., Beck R., 2007, A&A, 461, 455

Breitschwerdt D., McKenzie J. F., Völk H. J., 1991, A&A, 245, 79

Breitschwerdt D., McKenzie J. F., Völk H. J., 1993, A&A, 269, 54

Breitschwerdt D., de Avillez M. A., Baumgartner V., Dogiel V. A., 2012, in de Avillez M. A., ed., EAS Publ. Ser. Vol. 56, The Role of the Disk–Halo Interaction in Galaxy Evolution: Outflow vs. Infall?. EDP Sciences, Les Ulis, p. 333

Carilli C. L., Holdaway M. A., Ho P. T. P., de Pree C. G., 1992, ApJ, 399, L59

Carretti E., Haverkorn M., McConnell D., Bernardi G., McClure-Griffiths N. M., Cortiglioni S., Poppi S., 2010, MNRAS, 405, 1670

Cecil G., Bland-Hawthorn J., Veilleux S., Filippenko A. V., 2001, ApJ, 555, 338

Cecil G., Bland-Hawthorn J., Veilleux S., 2002, ApJ, 576, 745

Chyży K. T., Drzazga R. T., Beck R., Urbanik M., Heesen V., Bomans D. J., 2016, ApJ, 819, 39

Colbert E. J. M., Baum S. A., Gallimore J. F., O'Dea C. P., Christensen J. A., 1996, ApJ, 467, 551

Collins J. A., Rand R. J., Duric N., Walterbos R. A. M., 2000, ApJ, 536, 645

Condon J. J., 1992, ARA&A, 30, 575

Condon J. J., Helou G., Sanders D. B., Soifer B. T., 1996, ApJS, 103, 81

Condon J. J., Cotton W. D., Broderick J. J., 2002, AJ, 124, 675

Dahlem M., Dettmar R.-J., Hummel E., 1994, A&A, 290, 384

Dahlem M., Petr M. G., Lehnert M. D., Heckman T. M., Ehle M., 1997, A&A, 320, 731

Dahlem M., Ehle M., Ryder S. D., Vlajić M., Haynes R. F., 2005, A&A, 432, 475

Dale D. A., Helou G., 2002, ApJ, 576, 159

Dale D. A. et al., 2009, ApJ, 703, 517

Dorfi E. A., Breitschwerdt D., 2012, A&A, 540, A77

Draine B. T., 2011, Physics of the Interstellar and Intergalactic Medium. Princeton Univ. Press, Princeton, NJ

Dumke M., 1997, PhD thesis, Univ. Bonn, Bonn

Dumke M., Krause M., 1998, in Breitschwerdt D., Freyberg M. J., Trümper J., eds, Lecture Notes in Physics, Vol. 506, IAU Colloq. 166: The Local Bubble and Beyond. Springer-Verlag, Berlin, p. 555

Dumke M., Krause M., Wielebinski R., Klein U., 1995, A&A, 302, 691

Duric N., Irwin J., Bloemen H., 1998, A&A, 331, 428

Engelbracht C. W., Rieke G. H., Gordon K. D., Smith J.-D. T., Werner M. W., Moustakas J., Willmer C. N. A., Vanzi L., 2008, ApJ, 678, 804

Everett J. E., Zweibel E. G., Benjamin R. A., McCammon D., Rocks L., Gallagher J. S., III, 2008, ApJ, 674, 258

Ferrière K. M., 2001, Rev. Mod. Phys., 73, 1031
Fletcher A., 2010, in Kothes R., Landecker T. L., Willis A. G., eds, ASP Conf. Ser. Vol. 438, The Dynamic Interstellar Medium: A Celebration of the Canadian Galactic Plane Survey. Astron. Soc. Pac., San Francisco, p. 197
Gil de Paz A. et al., 2007, ApJS, 173, 185
Golla G., Hummel E., 1994, A&A, 284, 777
Gregory P. C., Condon J. J., 1991, ApJS, 75, 1011
Griffith M. R., Wright A. E., 1993, AJ, 105, 1666
Griffith M. R., Wright A. E., Burke B. F., Ekers R. D., 1995, ApJS, 97, 347
Haverkorn M., Heesen V., 2012, Space Sci. Rev., 166, 133
Haynes M. P., Giovanelli R., Roberts M. S., 1979, ApJ, 229, 83
Heald G. H., 2012, ApJ, 754, L35
Heald G., Williams A., Sridhar S. S., 2016, preprint (arXiv:1603.04722)
Heckman T. M., Borthakur S., 2016, ApJ, 822, 9
Heckman T. M., Lehnert M. D., Strickland D. K., Armus L., 2000, ApJS, 129, 493
Heckman T. M., Alexandroff R. M., Borthakur S., Overzier R., Leitherer C., 2015, ApJ, 809, 147
Heesen V., Beck R., Krause M., Dettmar R.-J., 2009a, A&A, 494, 563
Heesen V., Krause M., Beck R., Dettmar R.-J., 2009b, A&A, 506, 1123
Heesen V., Beck R., Krause M., Dettmar R.-J., 2011, A&A, 535, A79
Heesen V., Brinks E., Leroy A. K., Heald G., Braun R., Bigiel F., Beck R., 2014, AJ, 147, 103
Heesen V. et al., 2015, MNRAS, 447, L1
Heesen V., Dettmar R.-J., Krause M., Beck R., Stein Y., 2016, MNRAS, 458, 332 (HD16)
Heesen V. et al., 2018, MNRAS, 474, 5049
Henriksen R. N., Irwin J. A., 2016, MNRAS, 458, 4210
Ho L. C., Filippenko A. V., Sargent W. L. W., 1997, ApJS, 112, 315
Hodges-Kluck E. J., Bregman J. N., 2013, ApJ, 762, 12
Hummel E., Lesch H., Wielebinski R., Schlickeiser R., 1988, A&A, 197, L29
Hunter D. A. et al., 2012, AJ, 144, 134
Irwin J. A., English J., Sorathia B., 1999, AJ, 117, 2102
Irwin J. A. et al., 2011, MNRAS, 410, 1423
Irwin J. et al., 2012, AJ, 144, 43
Irwin J. A., Brar R. S., Saikia D. J., Henriksen R. N., 2013, MNRAS, 433, 2958
James P. A. et al., 2004, A&A, 414, 23
Karachentsev I. D. et al., 2003, A&A, 404, 93
Karachentsev I. D., Makarov D. I., Kaisina E. I., 2013, AJ, 145, 101
Kennicutt R. C., Evans N. J., 2012, ARA&A, 50, 531
Kennicutt R. C., Jr, Lee J. C., Funes José G. S. J., Sakai S., Akiyama S., 2008, ApJS, 178, 247
Kettenis M., van Langevelde H. J., Reynolds C., Cotton B., 2006, in Gabriel C., Arviset C., Ponz D., Enrique S., eds, ASP Conf. Ser. Vol. 351, Astronomical Data Analysis Software and Systems XV. Astron. Soc. Pac., San Francisco, p. 497
Krause M., 2009, Rev. Mex. Astron. Astrofis. Ser. Conf., 36, 25
Krause M., 2015, Highlights Astron., 16, 399
Krause M., Wielebinski R., Dumke M., 2006, A&A, 448, 133
Krause M. et al., 2017, preprint (arXiv:1712.03780)
Lee S.-W., Irwin J. A., 1997, ApJ, 490, 247
Li J. T. et al., 2016, MNRAS, 456, 1723
Lisenfeld U., Völk H. J., 2000, A&A, 354, 423
Longair M. S., 2011, High Energy Astrophysics. Cambridge Univ. Press, Cambridge
Mac Low M.-M., Ferrara A., 1999, ApJ, 513, 142
McMullin J. P., Waters B., Schiebel D., Young W., Golap K., 2007, in Shaw R. A., Hill F., Bell D. J., eds, ASP Conf. Ser. Vol. 376, Astronomical Data Analysis Software and Systems XVI. Astron. Soc. Pac., San Francisco, p. 127
Makarov D., Prugniel P., Terekhova N., Courtois H., Vauglin I., 2014, A&A, 570, A13
Mao S. A., Zweibel E., Fletcher A., Ott J., Tabatabaei F., 2015, ApJ, 800, 92
Martin C. L., 2005, ApJ, 621, 227

Middelberg E., Agudo I., Roy A. L., Krichbaum T. P., 2007, MNRAS, 377, 731
Mora S. C., Krause M., 2013, A&A, 560, A42
Moshir M. et al., 1990, BAAS, 22, 1325
Moustakas J., Kennicutt R. C., Jr, 2006, ApJS, 164, 81
Mulcahy D. D. et al., 2014, A&A, 568, A74
Mulcahy D. D., Fletcher A., Beck R., Mitra D., Scaife A. M. M., 2016, A&A, 592, A123
Mulcahy D. D., Beck R., Heald G. H., 2017, A&A, 600, A6
Murray N., Quataert E., Thompson T. A., 2005, ApJ, 618, 569
Niklas S., Beck R., 1997, A&A, 320, 54
Niklas S., Klein U., Wielebinski R., 1997, A&A, 322, 19
Oosterloo T., Fraternali F., Sancisi R., 2007, AJ, 134, 1019
Parker E. N., 1992, ApJ, 401, 137
Pence W. D., 1981, ApJ, 247, 473
Perley R. A., Butler B. J., 2013, ApJS, 204, 19
Pietrzyński G. et al., 2006, AJ, 132, 2556
Ptuskin V. S., Voelk H. J., Zirakashvili V. N., Breitschwerdt D., 1997, A&A, 321, 434
Rand R. J., Wood K., Benjamin R. A., Meidt S. E., 2011, ApJ, 728, 163
Rau U., Cornwell T. J., 2011, A&A, 532, A71
Recchia S., Blasi P., Morlino G., 2016a, MNRAS, 462, L88
Recchia S., Blasi P., Morlino G., 2016b, MNRAS, 462, 4227
Reuter H.-P., Krause M., Wielebinski R., Lesch H., 1991, A&A, 248, 12
Rice W., Lonsdale C. J., Soifer B. T., Neugebauer G., Kopan E. L., Lloyd L. A., de Jong T., Habing H. J., 1988, ApJS, 68, 91
Rieger F. M., de Oña-Wilhelmi E., Aharonian F. A., 2013, Front. Phys., 8, 714
Robitaille T. P., Rossa J., Bomans D. J., van der Marel R. P., 2007, A&A, 464, 541
Rossa J., Dettmar R.-J., 2003a, A&A, 406, 493
Rossa J., Dettmar R.-J., 2003b, A&A, 406, 505
Rupen M. P., van Gorkom J. H., Knapp G. R., Gunn J. E., Schneider D. P., 1987, AJ, 94, 61
Rupke D. S., Veilleux S., Sanders D. B., 2005, ApJS, 160, 115
Salem M., Bryan G. L., 2014, MNRAS, 437, 3312
Samui S., Subramanian K., Srianand R., 2010, MNRAS, 402, 2778
Sanders D. B., Mazzarella J. M., Kim D.-C., Surace J. A., Soifer B. T., 2003, AJ, 126, 1607
Sault R. J., Teuben P. J., Wright M. C. H., 1995, in Shaw R. A., Payne H. E., Hayes J. J. E., eds, ASP Conf. Ser. Vol. 77, Astronomical Data Analysis Software and Systems IV. Astron. Soc. Pac., San Francisco, p. 433
Sault R. J., Staveley-Smith L., Brouw W. N., 1996, A&AS, 120, 375
Shafi N., Oosterloo T. A., Morganti R., Colafrancesco S., Booth R., 2015, MNRAS, 454, 1404
Sofue Y., Wakamatsu K.-I., Malin D. F., 1994, AJ, 108, 2102
Soida M., Krause M., Dettmar R.-J., Urbanik M., 2011, A&A, 531, A127
Soifer B. T., Boehmer L., Neugebauer G., Sanders D. B., 1989, AJ, 98, 766
Stil J. M., Krause M., Beck R., Taylor A. R., 2009, ApJ, 693, 1392
Strickland D. K., Heckman T. M., Colbert E. J. M., Hoopes C. G., Weaver K. A., 2004, ApJS, 151, 193
Strong A. W., Moskalenko I. V., Ptuskin V. S., 2007, Annu. Rev. Nucl. Part. Sci., 57, 285
Sukumar S., Allen R. J., 1991, ApJ, 382, 100
Tabatabaei F. S. et al., 2013a, A&A, 552, A19
Tabatabaei F. S., Berkhuijsen E. M., Frick P., Beck R., Schinnerer E., 2013b, A&A, 557, A129
Tabatabaei F. S. et al., 2017, ApJ, 836, 185
Tüllmann R., Dettmar R.-J., Soida M., Urbanik M., Rossa J., 2000, A&A, 364, L36
Tully R. B., Fisher J. R., 1988, Catalog of Nearby Galaxies. Cambridge Univ. Press, Cambridge
van Haarlem M. P. et al., 2013, A&A, 556, A2
Veilleux S., Kim D.-C., Sanders D. B., Mazzarella J. M., Soifer B. T., 1995, ApJS, 98, 171
Voigtländer P., Kamphuis P., Marcelin M., Bomans D. J., Dettmar R.-J., 2013, A&A, 554, A133
Vollmer B., Nehlig F., Ibata R., 2016, A&A, 586, A98

Wells B. S., 1997, PASA, 14, 292

Westmeier T., Koribalski B. S., Braun R., 2013, MNRAS, 434, 3511

Westmoquette M. S., Smith L. J., Gallagher J. S., III, 2011, MNRAS, 414, 3719

White R. L., Becker R. H., 1992, ApJS, 79, 331

Wiegert T. et al., 2015, AJ, 150, 81

Wilson W. E. et al., 2011, MNRAS, 416, 832

Wright A. E., Griffith M. R., Burke B. F., Ekers R. D., 1994, ApJS, 91, 111

Yoast-Hull T. M., Everett J. E., Gallagher J. S., III, Zweibel E. G., 2013, ApJ, 768, 53

Young J. S., Allen L., Kenney J. D. P., Lesser A., Rownd B., 1996, AJ, 112, 1903

Zschaechner L. K., Rand R. J., Heald G. H., Gentile G., Józsa G., 2012, ApJ, 760, 37

Zschaechner L. K., Rand R. J., Walterbos R., 2015, ApJ, 799, 61

SUPPORTING INFORMATION

Supplementary data are available at *MNRAS* online.

Appendix D. Image atlas.

Please note: Oxford University Press is not responsible for the content or functionality of any supporting materials supplied by the authors. Any queries (other than missing material) should be directed to the corresponding author for the article.

APPENDIX A: PHYSICAL PARAMETERS

In order to calculate the synchrotron and IC losses of the CREs, we need to make estimates of both the magnetic field strength and the radiation energy density. The magnetic field strength is calculated assuming energy equipartition between the cosmic rays and the magnetic field using the revised equipartition formula of Beck & Krause ([2005](#)). We calculate the radio continuum surface intensity $I_1 = S_1/(\pi r_\star^2)$ (using the 1.4-GHz flux densities) and use this as an input for the program BFIELD, assuming a path-length of 1 kpc, an inclination angle of $i = 0°$, a polarization degree of 10 per cent, a proton-to-electron ratio of $K_0 = 100$, and a non-thermal radio spectral index of $\alpha_{nt} = -1$.[10] Resulting magnetic field strengths in the mid-plane are tabulated in Table [6](#).

The IRF radiation energy density is the sum of the starlight radiation energy density and the total infrared radiation energy density from dust. Following Draine ([2011](#)), the starlight radiation energy density is scaled to the total infrared radiation energy density as $U_{star} = 1.73 \times U_{TIR}$, so that we find the IRF energy density as $U_{IRF} = U_{TIR} + U_{star} = 2.73 \times U_{TIR}$.[11] The total infrared radiation energy density is then calculated as $U_{TIR} = L_{TIR}/(2\pi r_\star^2 c)$, where L_{TIR} is the total infrared luminosity and c is the speed of light:

$$U_{TIR}(10^{-13}\,\mathrm{erg\,cm^{-3}}) = 175 \times \frac{L_{TIR}(10^{43}\,\mathrm{erg\,s^{-1}})}{\pi r_\star^2(\mathrm{kpc})^2}. \tag{A1}$$

The total infrared luminosities are derived either from *Spitzer* (if available) or *IRAS* data using the prescriptions by Dale & Helou ([2002](#)). The *Spitzer* flux densities are from Engelbracht et al. ([2008](#), NGC 3079) and Dale et al. ([2009](#), NGC 4631 and 7090). The *IRAS*

---

[10] The program BFIELD is available at http://www3.mpifr-bonn.mpg.de/staff/mkrause/

[11] In Draine ([2011](#)), the ratio of 1.73 of stellar radiation energy density to far-infrared radiation energy density is presented. We have used the total infrared luminosity instead in order to also include the emission from the hot dust.

flux densities are from Rice et al. ([1988](#), NGC 55), Soifer et al. ([1989](#), NGC 3044), Moshir et al. ([1990](#), NGC 7462), and Sanders et al. ([2003](#), NGC 253, 891, 3628, 4565, 4666, and 5775).

The ratio of IRF to magnetic field energy density U_{IRF}/U_B, with $U_B = B_0^2/(8\pi)$, is assumed to be constant everywhere and lies between 0.02 (NGC 7462) and 0.25 (NGC 253). The total radiation energy density is then $U_{rad} = U_{IRF} + U_{CMB}$, where $U_{CMB} = 4.1 \times 10^{-13}\,\mathrm{erg\,cm^{-3}}$ is the radiation energy density of the CMB. The ratio of radiation energy density to magnetic energy density is then also the ratio of IC to synchrotron losses. In our sample galaxies, the ratio lies between 0.15 (NGC 3079) and 0.30 (NGC 253); hence, synchrotron losses dominate. We tabulate the radiation energy densities in Table [6](#).

APPENDIX B: INTENSITY MODELS

Following Dumke et al. ([1995](#)), we used analytical functions that allow the fitting of vertical radio continuum emission profiles with one- or two-component Gaussian or exponential functions, where the instrumental PSF is assumed to be of Gaussian shape, which is exact for interferometric maps (synthesized beam). In addition to the PSF, a correction for projected disc emission can be added, for instance by fitting a Gaussian and adding the FWHM in quadrature. We have done this, so that the combined resolution is $FWHM_{comb} = \sqrt{FWHM^2 + (\cos(i) \cdot FWHM_{disc})^2}$. The effective beam size is then $b = 0.5 \cdot FWHM_{comb}/\sqrt{2\ln(2)} \approx 0.425 \cdot FWHM_{comb}$. The effective beam sizes for our sample galaxies can be found in Table [B1](#). For an exponential profile, we fit the following function:

$$W_{exp}(z) = \frac{w_0}{2} \exp\left(-\frac{z^2}{2b^2}\right)$$
$$\times \left[\exp\left(\frac{b^2 - zz_0}{\sqrt{2}bz_0}\right)^2 \mathrm{erfc}\left(\frac{b^2 - zz_0}{\sqrt{2}bz_0}\right) \right.$$
$$\left. + \exp\left(\frac{b^2 + zz_0}{\sqrt{2}bz_0}\right)^2 \mathrm{erfc}\left(\frac{b^2 + zz_0}{\sqrt{2}bz_0}\right) \right], \tag{B1}$$

where b is the effective beam size, w_0 is the maximum of the distribution, and z_0 is the (exponential) scale height. We have introduced the complementary error function as

$$\mathrm{erfc}(x) = 1 - \mathrm{erf}(x) = \frac{2}{\sqrt{\pi}} \int_0^\infty \exp(-r^2)\mathrm{d}r. \tag{B2}$$

Table B1. Effective beam sizes.

Galaxy	i (°)	$FWHM_{disc}$ (kpc)	$FWHM_{comb}$ (kpc)	b (kpc)
N 55	85.0	2.2	0.44	0.18
N 253	78.5	6.5	1.43	0.60
N 891	89.0	11.6	0.91	0.38
N 3044	90.0	3.8	0.73	0.31
N 3079	88.0	9.0	0.88	0.37
N 3628	87.0	12.0	0.95	0.40
N 4565	90.0	40.0	1.62	0.68
N 4631	85.0	6.3	0.97	0.41
N 4666	76.0	11.0	3.39	1.42
N 5775	84.0	15.0	1.93	0.81
N 7090	89.0	5.5	0.74	0.31
N 7462	90.0	5.5	0.95	0.40

Table B2. Exponential (top half of the table) and Gaussian (bottom half) fits to the vertical profiles of the non-thermal radio continuum intensities. In the top half of the table, $w20n1$, $w20n2$, $w20s1$, and $w20s2$ are the intensities at ν_1 (1.4 or 1.5 GHz) in the northern and southern halo for the thin and the thick disc, respectively. Similarly, $w6n1$, $w6n2$, $w6s1$, and $w6s2$ are the values at ν_2 (mostly ≈ 5 GHz, except N 5775 where $\nu_2 = 8.46$ GHz). The corresponding exponential scale heights are $h20n1$, $h20n2$, $h20s1$, and $h20s2$. In the bottom half of the table, the analogue values with an additional 'g' are presented for Gaussian fits to the intensities. Reduced χ^2 are also presented for each fit.

Galaxy	$w20n1$ (μJy beam^{-1})	$w20n2$	$h20n1$ (kpc)	$h20n2$	χ^2	$w6n1$ (μJy beam^{-1})	$w6n2$	$h6n1$ (kpc)	$h6n2$	χ^2
N 55	6048 ± 233	292 ± 239	0.36 ± 0.03	2.03 ± 1.46	0.63	3807 ± 51	260 ± 37	0.22 ± 0.01	1.72 ± 0.22	0.41
N 253	–	16991 ± 1242	0.44 ± 0.06	1.26 ± 0.07	5.86	–	6023 ± 389	0.38 ± 0.06	1.14 ± 0.04	5.85
N 891	33576 ± 5493	11463 ± 493	0.10 ± 0.05	1.33 ± 0.02	1.59	17675 ± 7801	3258 ± 137	0.11 ± 0.05	1.30 ± 0.02	0.82
N 3044	2481 ± 58	113 ± 25	0.60 ± 0.30	3.64 ± 0.95	0.39	1351 ± 90	202 ± 63	0.32 ± 0.04	1.47 ± 0.26	0.75
N 3079	3598 ± 106	111 ± 149	0.77 ± 0.05	5.14 ± 8.86	0.13	1051 ± 254	519 ± 311	0.43 ± 0.11	1.00 ± 0.19	0.22
N 3628	7950 ± 1503	2949 ± 208	0.10 ± 0.10	1.23 ± 0.05	1.63	4160 ± 506	932 ± 63	0.10 ± 0.10	1.16 ± 0.04	1.40
N 4565	–	1799 ± 164	–	1.90 ± 0.10	5.00	–	689 ± 44	–	1.63 ± 0.06	2.08
N 4631	31222 ± 1567	6085 ± 387	0.47 ± 0.03	2.24 ± 0.07	0.48	16976 ± 1112	2469 ± 158	0.33 ± 0.02	1.70 ± 0.05	0.60
N 4666	13439 ± 4252	16167 ± 1509	0.41^a	1.51 ± 0.05	0.69	18535 ± 918	3714 ± 171	0.23^a	1.54 ± 0.03	0.13
N 5775	5364 ± 164	968 ± 97	0.70 ± 0.03	2.72 ± 0.12	0.21	5827 ± 538	560 ± 56	0.10 ± 0.30	1.27 ± 0.06	0.96
N 7090	1585 ± 201	616 ± 76	0.31 ± 0.07	2.07 ± 0.18	0.93	576 ± 85	124 ± 44	0.32 ± 0.09	1.96 ± 0.50	2.23
N 7462	–	864 ± 50	–	0.99 ± 0.04	1.72	–	223 ± 17	–	0.86 ± 0.06	2.31
	$w20s1$	$w20s2$	$h20s1$	$h20s2$	χ^2	$w6s1$	$w6s2$	$h6s1$	$h6s2$	χ^2
N 55	5067 ± 809	1859 ± 401	0.20 ± 0.05	1.06 ± 0.14	2.15	4136 ± 602	231 ± 71	0.17 ± 0.02	2.01 ± 0.71	3.92
N 253	–	15587 ± 625	0.44 ± 0.06	1.33 ± 0.04	1.70	–	5484 ± 172	0.38 ± 0.06	1.28 ± 0.02	1.47
N 891	43174 ± 2381	9433 ± 195	0.10 ± 0.05	1.25 ± 0.01	0.33	13587 ± 3081	2797 ± 169	0.18 ± 0.04	1.24 ± 0.03	1.11
N 3044	1786 ± 106	849 ± 125	0.38 ± 0.05	1.30 ± 0.08	0.30	1223 ± 76	318 ± 90	0.33 ± 0.05	1.15 ± 0.14	0.44
N 3079	3511 ± 182	513 ± 143	0.72 ± 0.07	3.41 ± 0.63	0.98	1100 ± 61	447 ± 74	0.49 ± 0.05	1.54 ± 0.10	0.24
N 3628	5082 ± 371	56 ± 238	0.73 ± 0.12	594 ± 4.e5	3.13	3296 ± 374	1229 ± 64	0.10 ± 0.10	0.87 ± 0.02	0.57
N 4565	1531 ± 312	505 ± 159	0.80 ± 0.80	3.11 ± 0.66	3.71	696 ± 177	500 ± 47	0.25	1.75 ± 0.10	0.91
N 4631	26395 ± 1537	14554 ± 476	0.32 ± 0.02	1.47 ± 0.02	0.11	17953 ± 3730	6752 ± 362	0.19 ± 0.05	1.13 ± 0.02	0.53
N 4666	25119 ± 3712	9393 ± 967	0.41^a	2.01 ± 0.08	1.06	17737 ± 3418	3487 ± 569	0.23^a	1.70 ± 0.11	2.20
N 5775	6593 ± 2164	1857 ± 293	0.35 ± 0.15	1.91 ± 0.12	2.21	7993 ± 318	269 ± 25	0.10 ± 0.30	2.03 ± 0.80	0.62
N 7090	1500 ± 129	443 ± 27	0.40 ± 0.06	1.53 ± 0.39	1.96	439 ± 53	148 ± 13	0.29 ± 0.10	1.14 ± 0.44	2.17
N 7462	–	1164 ± 103	–	0.88 ± 0.05	4.59	–	257 ± 27	–	0.90 ± 0.08	5.52
	$w20gn1$	$w20gn2$	$h20gn1$	$h20gn2$	χ^2	$w6gn1$	$w6gn2$	$h6gn1$	$h6gn2$	χ^2
N 55	3877 ± 178	568 ± 69	0.51 ± 0.02	1.71 ± 0.11	0.91	2364 ± 157	211 ± 19	0.39 ± 0.02	2.09 ± 0.14	1.51
N 253	8944 ± 5027	3323 ± 5474	1.57 ± 0.50	2.92 ± 1.25	3.64	3666 ± 439	994 ± 439	1.27 ± 0.21	3.16 ± 0.47	6.03
N 891	13568 ± 2341	3444 ± 275	0.71 ± 0.10	3.10 ± 0.07	5.23	6408 ± 910	1007 ± 70	0.60 ± 0.07	2.99 ± 0.07	3.54
N 3044	1561 ± 110	255 ± 46	0.84 ± 0.06	2.67 ± 0.23	2.20	920 ± 90	125 ± 20	0.55 ± 0.05	2.38 ± 0.21	2.10
N 3079	2208 ± 164	646 ± 99	0.86 ± 0.07	2.44 ± 0.15	1.34	928 ± 29	222 ± 17	0.67 ± 0.03	2.04 ± 0.06	0.18
N 3628	4650 ± 1512	1329 ± 135	0.37 ± 0.14	2.35 ± 0.11	3.57	2959 ± 1327	423 ± 33	0.24 ± 0.11	2.24 ± 0.08	2.47
N 4565	–	1243 ± 92	–	2.15 ± 0.14	2.74	–	494 ± 39	–	1.65 ± 0.13	1.72
N 4631	19405 ± 1910	2617 ± 200	0.99 ± 0.06	4.33 ± 0.14	3.80	9677 ± 1201	891 ± 83	0.76 ± 0.06	3.60 ± 0.14	4.80
N 4666	19698 ± 1657	3949 ± 198	0.96 ± 0.10	3.81 ± 0.05	0.11	7709 ± 877	720 ± 116	1.07 ± 0.14	4.11 ± 0.19	0.61
N 5775	3609 ± 246	446 ± 40	1.30 ± 0.08	5.14 ± 0.21	1.71	3742 ± 1744	204 ± 11	0.24 ± 0.12	2.77 ± 0.06	0.24
N 7090	1172 ± 47	353 ± 11	0.62 ± 0.03	3.27 ± 0.07	0.28	398 ± 28	74 ± 7	0.60 ± 0.04	3.10 ± 0.19	0.97
N 7462	–	536 ± 77	–	1.62 ± 0.15	13.9	–	149 ± 4	–	1.38 ± 0.03	0.47
	$w20gs1$	$w20gs2$	$h20gs1$	$h20gs2$	χ^2	$w6gs1$	$w6gs2$	$h6gs1$	$h6gs2$	χ^2
N 55	3728 ± 423	947 ± 96	0.40 ± 0.04	1.84 ± 0.11	2.84	2630 ± 453	188 ± 33	0.30 ± 0.04	2.26 ± 0.35	7.23
N 253	6561 ± 1213	5426 ± 1456	1.22 ± 0.24	2.74 ± 0.23	0.82	3296 ± 146	1231 ± 99	1.19 ± 0.06	3.22 ± 0.09	0.74
N 891	13171 ± 2308	2421 ± 236	0.75 ± 0.10	3.06 ± 0.08	6.90	6241 ± 832	783 ± 65	0.65 ± 0.07	2.93 ± 0.08	3.95
N 3044	1476 ± 73	372 ± 23	0.69 ± 0.03	2.50 ± 0.07	0.68	905 ± 60	155 ± 18	0.57 ± 0.04	2.15 ± 0.13	1.05
N 3079	2284 ± 184	400 ± 41	1.17 ± 0.07	4.62 ± 0.27	2.91	885 ± 71	198 ± 24	0.85 ± 0.07	3.00 ± 0.17	1.69
N 3628	3792 ± 1026	1389 ± 252	0.47 ± 0.16	1.92 ± 0.14	4.61	1890 ± 252	427 ± 32	0.40 ± 0.06	1.89 ± 0.06	0.98
N 4565	–	1201 ± 80	–	1.77 ± 0.09	1.68	–	522 ± 62	–	1.21 ± 0.17	2.22
N 4631	20322 ± 2099	5066 ± 430	0.83 ± 0.08	3.12 ± 0.10	2.50	10913 ± 837	1949 ± 107	0.65 ± 0.04	2.62 ± 0.05	1.14
N 4666	25617 ± 6272	3132 ± 215	0.74 ± 0.20	4.52 ± 0.10	0.45	(1.1 ± 2.1)e5	1125 ± 56	0.06 ± 1.20	3.92 ± 0.06	0.18
N 5775	3573 ± 510	505 ± 83	1.16 ± 0.15	4.49 ± 0.29	5.32	2343 ± 621	106 ± 11	0.45 ± 0.12	4.08 ± 0.22	1.78
N 7090	1206 ± 105	190 ± 26	0.69 ± 0.06	190 ± 26	2.17	389 ± 28	54 ± 6	0.50 ± 0.04	2.84 ± 0.24	0.80
N 7462	–	731 ± 29	–	1.50 ± 0.03	1.22	–	172 ± 2	–	1.46 ± 0.01	0.10

Notes. Exponential scale heights in the southern halo of NGC 7090 are from HD16.
^{a}Average scale height of the sample, since the exponential scale height in the thin disc in NGC 4666 is unconstrained.

And for a Gaussian intensity profile, we fit the following function:

$$W_{\text{Gauss}}(z) = \frac{w_o z_0}{\sqrt{2b^2 + z_0^2}} \exp\left(-\frac{z^2}{2b^2 + z_0^2}\right). \tag{B3}$$

Again, b is the effective beam size, w_0 the maximum of the distribution, and z_0 the (Gaussian) scale height. We have fitted for a thin and a thick disc in all those cases where this provided a better fit than a single thick disc. The resulting fit parameters

Table C1. Additional maps produced in our study.

Galaxy	Telescope	ν (GHz)	θ_{FWHM} (arcsec)	σ_{rms} (mJy beam^{-1})	S_ν (mJy)
N 55	Parkes	4.80	255.0	1.50	333
N 891	Effelsberg	4.85	147.0	0.50	281
N 4157	VLA	1.49	25.1×13.7	0.10	185
N 4217	VLA	4.86	15.8×10.9	0.04	44
N 4631	Effelsberg	4.85	147.0	0.50	472
N 4631	VLA	1.35	52.0	0.04	1201
N 4631	VLA	1.65	52.0	0.05	975
N 4634	VLA	4.86	15.4×13.6	0.06	14

Notes. S_ν denotes the integrated flux density of each galaxy.

are presented in Table B2. Here, the maxima of the exponential thin and thick disc at *L* band in the northern halo are $w20n1$ and $w20n2$, with the corresponding scale heights of $h20n1$ and $h20n2$. Similarly, at *C* band, the maxima are $w6n1$ and $w6n2$ with scale heights of $h6n1$ and $h6n2$. For Gaussian fits, the same parameters at *L* band are $w20gn1$, $w20gn2$, $h20gn1$, and $h20gn2$. The parameters for *C* band and the southern haloes are defined in a similar way.

Using these fits, one can now construct the intensity models. For instance, the resulting (normalized) intensity model for *C* band ($\nu = \nu_2$) and an exponential intensity profile in the northern halo is

$$I_\nu(z) = \frac{w6n1 \cdot \exp(-z/h6n1) + w6n2 \cdot \exp(-z/h6n2)}{w6n1 + w6n2}. \quad (B4)$$

The other cases can be calculated accordingly.

APPENDIX C: ADDITIONAL RADIO CONTINUUM MAPS

As part of our study, we have obtained several additional radio continuum maps, which we present in this appendix. We will make these maps publicly available (as well as all the other radio continuum maps in this paper); see Table C1 for the map properties.[12]

---

[12] The maps will be made available on the website of the Centre de Données astronomiques de Strasbourg (CDS) (http://cds.u-strasbg.fr).

For four galaxies (NGC 55, 253, 891, and 4631), we have used single-dish maps, to correct for the missing zero-spacing flux where necessary. The Effelsberg maps of NGC 253 and 4631 were already presented in Heesen et al. (2009a) and Mora & Krause (2013), respectively, and the Effelsberg map of NGC 891 was already presented in Dumke (1997). We present these maps for completeness here again in Fig. C1. The 4.80-GHz map of NGC 55 obtained with the 64-m Parkes telescope is so far unpublished and shown here also in Fig. C1.

Furthermore, we show in Fig. C2 two maps of NGC 4631 at 1.35 and 1.65 GHz observed with the VLA in D-configuration (Beck, private communication). The data were observed in 1996 August, with 12-h on-source (ID: AG486) and reduced in standard fashion with AIPS. The maps have an angular resolution of 52 arcsec, so that we did not use them in the analysis, but they also show the halo of this galaxy very well. Lastly, we obtained maps of three further edge-on galaxies observed with the VLA (NGC 4157, 4217, and 4634), which we present in Fig. C3. We reduced the data as described in Section 2, but since we had only one frequency available and no spectral index map, we did not use them in the analysis. The maps of NGC 4157 and 4217 were created by re-reducing archive data (IDs AI23, AF85, AH457, and AS392 for NGC 4157 and ID AM573 for NGC 4217). The map of NGC 4634 was created by using so far unpublished data from the VLA (ID: AD538).
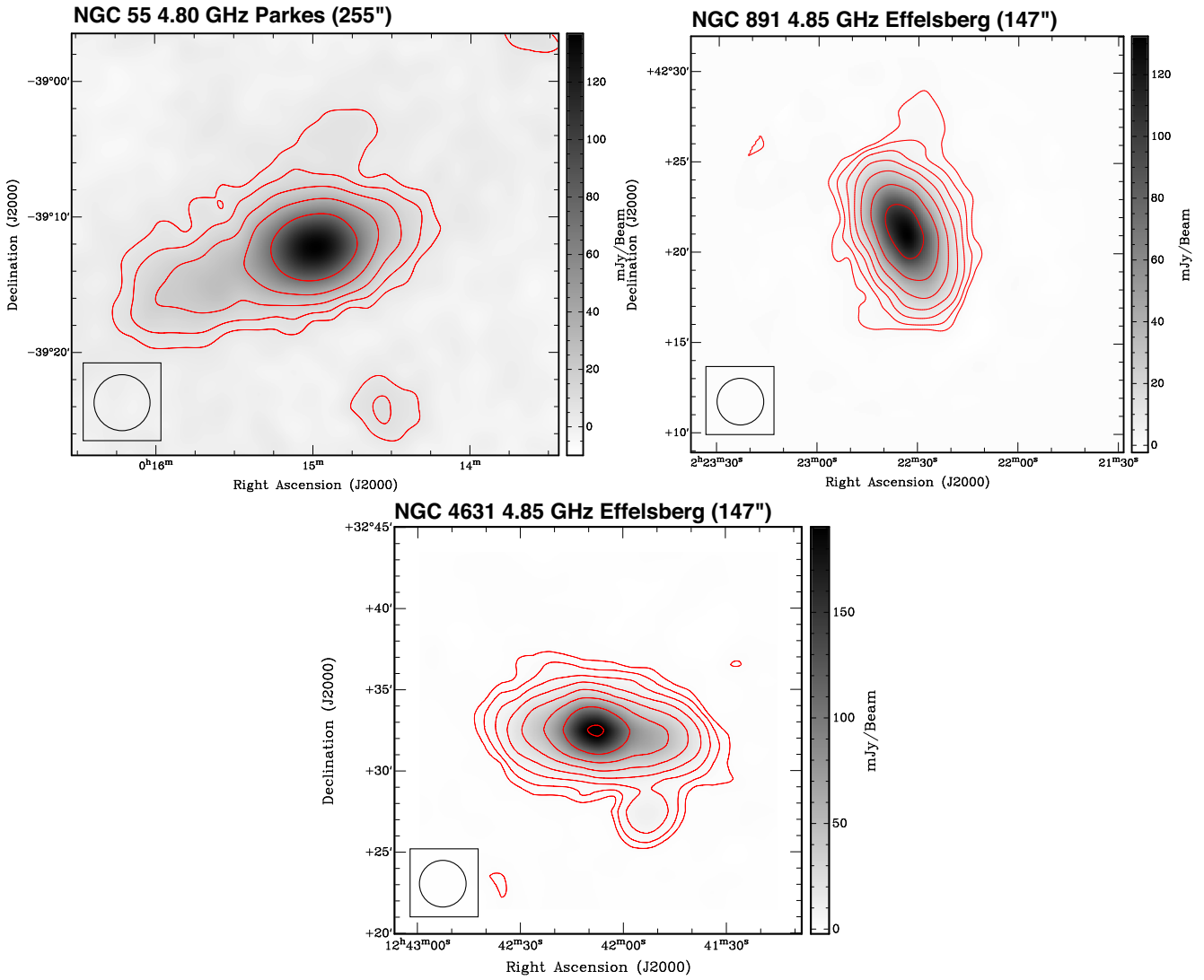
Figure C1. Single-dish maps of NGC 55 (top left), NGC 891 (top right), and NGC 4631 (bottom). Contours show the radio continuum emission at levels of $3\sigma \cdot 2^n$ ($n = 0, 1, 2, \dots$). The size of the primary beam is shown in the bottom-left corner.
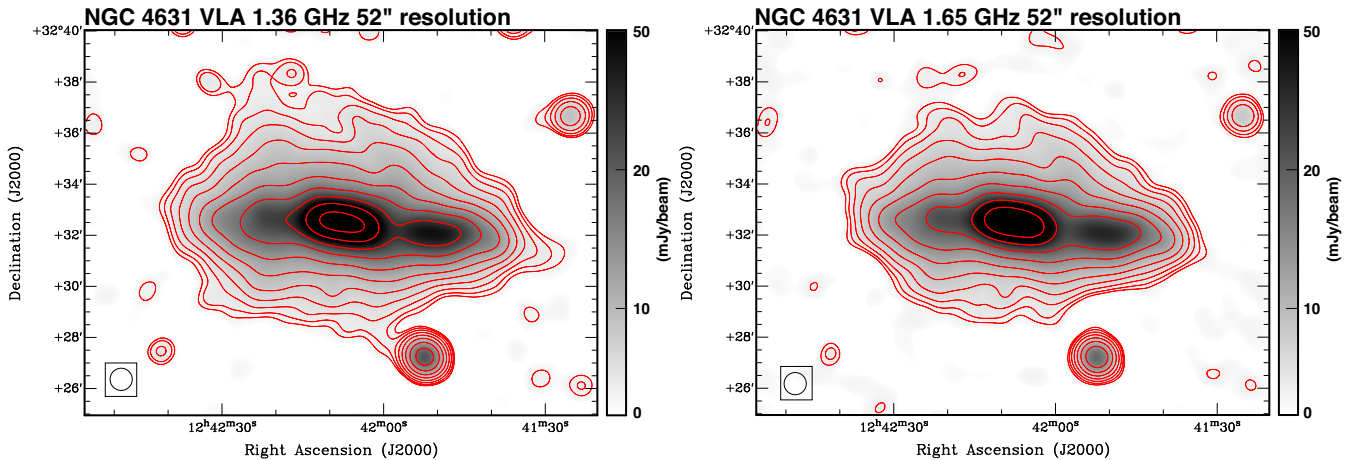

Figure C2. VLA maps of NGC 4631 at 1.37 GHz (left) and 1.65 GHz (right). Contours show the radio continuum emission at levels of $3\sigma \cdot 2^n$ ($n = 0, 1, 2, \dots$). The size of the synthesized beam is shown in the bottom-left corner.
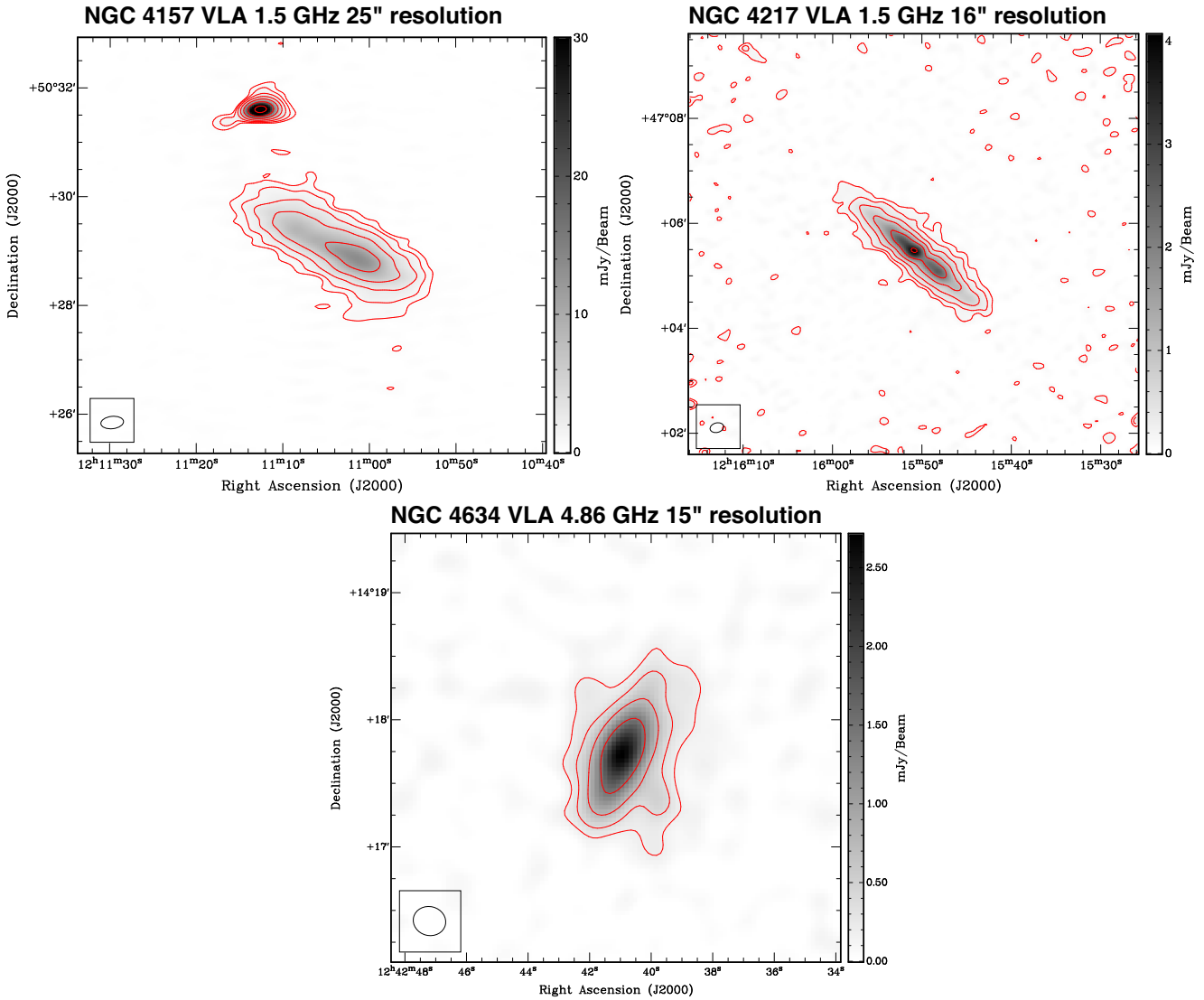
Figure C3. VLA maps of NGC 4157 (top left), NGC 4217 (top right), and NGC 4634 (bottom). Contours show the radio continuum emission at levels of $3\sigma \cdot 2^n$ ($n = 0, 1, 2, \dots$). The size of the synthesized beam is shown in the bottom-left corner.

APPENDIX D: IMAGE ATLAS

In this appendix, we present maps and vertical profiles for individual galaxies. Each page shows results for one galaxy. As an example, we show in Fig. D1 results for NGC 55.[13] The top row shows maps of the radio continuum emission at *L* and *C* band (1.4 and 5 GHz, except for NGC 5775 where instead of a *C*-band map we show an *X*-band map at 8.5 GHz) and the thermal radio continuum emission at 5 GHz (again, with the exception of NGC 5775, where we show the emission at *X* band instead). The second row shows thermal fraction at *C* band (again except for NGC 5775 where this is at *X* band), the non-thermal radio spectral index between *L* and *C* band (for NGC 5775 between *L* and *X* band), and the corresponding error of the non-thermal radio spectral index. In the radio maps, contours show the radio continuum emission at levels of (3, 6, 12, 24, 48, 96) × σ, where σ is the rms noise of the map. For the thermal radio continuum map, we use the same contours as of the radio

continuum map of either *C* or *X* band. In the first and second rows, the size of the synthesized beam is shown in the bottom-left corner and all maps are rotated so that the major axis is horizontal. In panels (c)–(f), a mask has been applied (Section 2.3).

The third row shows vertical profiles of the non-thermal radio continuum intensities, vertical non-thermal intensity model profiles at one frequency, and vertical profiles of the non-thermal radio spectral index. Panel (g) shows exponential (solid) and Gaussian fits (dashed lines) to the data, panel (h) shows model intensity profiles, and panel (i) shows radio spectral index profiles. The fourth row shows the reduced χ^2 of the cosmic ray transport model in the northern halo, in the southern halo, and the vertical model profile of the magnetic field strength. In panels (j) and (k), contours show $\chi^2_{\rm int,min} + 1$ for the intensity fitting (solid lines) and $\chi^2_{\rm spix,min} + 1$ for spectral index fitting (dashed lines). The colour scale shows the total reduced χ^2 (sum of intensity and spectral index fitting). The best-fitting models (with uncertainties) lie in the intersection of the two contours and are marked by yellow stars. In panel (l), the grey shaded area indicates the uncertainty of the magnetic field model.

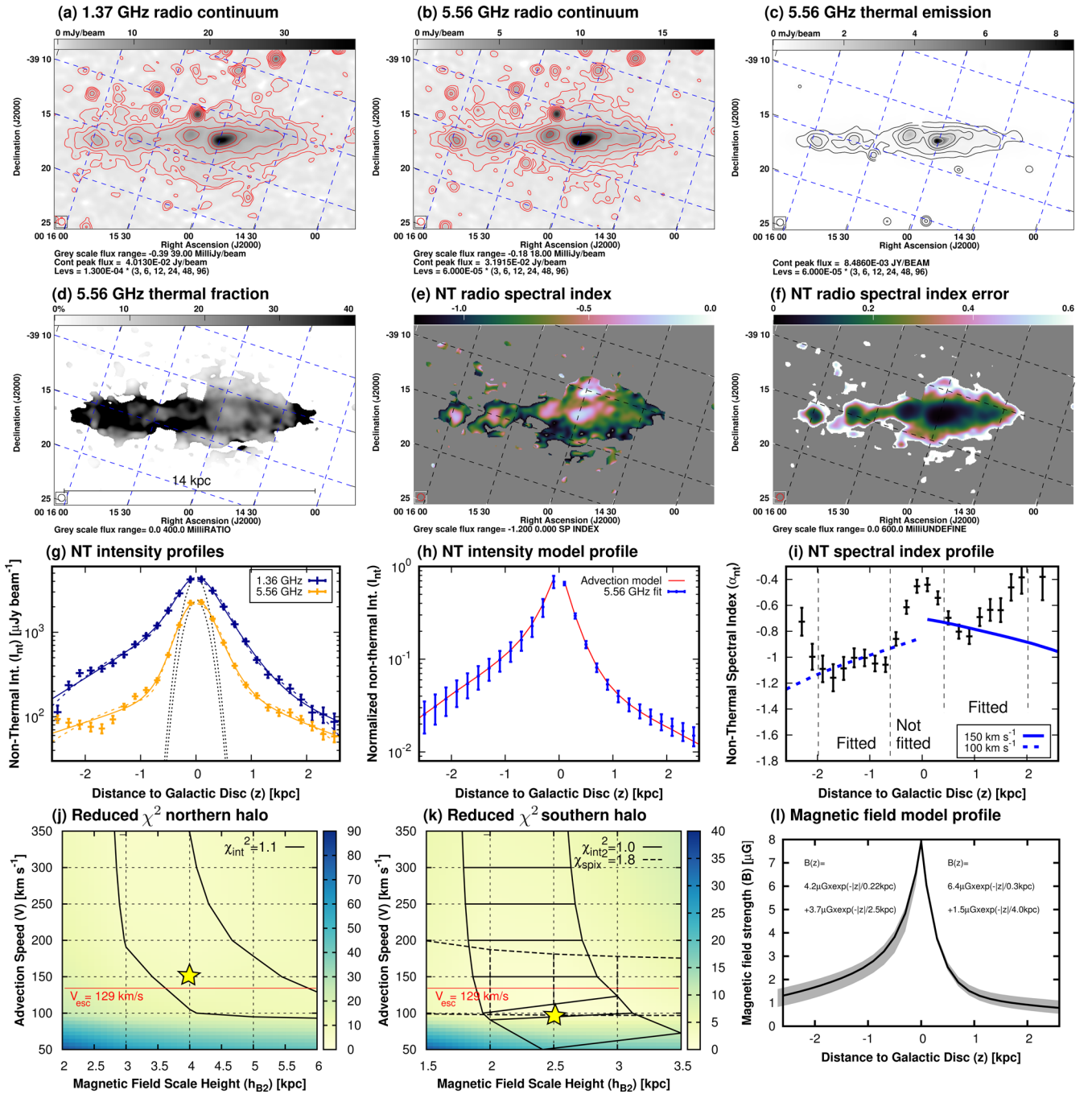[13] The complete image atlas (12 images) is available in the online journal.

Figure D1. NGC 55. (a) Radio continuum emission at 1.37 GHz. (b) Radio continuum emission at 5.56 GHz. (c) Thermal radio continuum emission at 5.56 GHz. Contours in panels (a) and (b) are at $(3, 6, 12, 24, 48,$ and $96) \times \sigma$, where σ is the rms map noise. In panel (c), the same contour levels as in panel (b) are used. (d) Thermal fraction at 5.56 GHz, where the grey-scale ranges from 0 to 40 per cent. (e) Non-thermal radio spectral index between 1.37 and 5.56 GHz, where the colour scale ranges from -1.2 to 0. (f) Error of the non-thermal radio spectral index, where the colour scale ranges from 0 to 0.6. Panels (a)–(f) are rotated so that the major axis (PA $= 108°$) is horizontal and the synthesized beam is shown in the bottom-left corner. (g) Vertical non-thermal intensity profiles at both frequencies, where solid lines show two-component exponential fits and dashed lines two-component Gaussian fits. (h) Normalized non-thermal vertical intensity model profile at 5.56 GHz with best-fitting advection model. (i) Vertical non-thermal radio spectral index profiles with best-fitting advection model. (j) Reduced χ^2 in the northern halo as a function of advection speed and magnetic field scale height in the thick disc. (k) Same as panel (j) but in the southern halo. The red lines in panels (j) and (k) show the escape velocity near the mid-plane. (l) Vertical magnetic field model profile. (The complete image atlas (12 images) is available in the online journal.)

This paper has been typeset from a TEX/LATEX file prepared by the author.